TECHNISCHE UNIVERSITÄT WIEN
Vienna University of Technology

DIPLOMARBEIT

Development and optimization of a biosensor device based on microwave split-ring resonators

Ausgeführt am Institut für

ANALYSIS AND SCIENTIFIC COMPUTING

TECHNISCHE UNIVERSITÄT WIEN

unter der Anleitung von

ao. Univ.-Prof. Dipl.-Ing. DDDr. Frank Rattay

und

Dr. Martin Brandl
Zentrum für Integrierte Sensorsysteme, Donau Universität Krems

durch

Lisa-Marie Wagner
Mittergasse 4
3620 Spitz

Krems an der Donau, 3.8.2017

DANKSAGUNG

Hiermit möchte ich mich bei all jenen bedanken, die mich während meiner Studienzeit unterstützt haben.

Ein besonderer Dank gilt meinem Betreuer Dr. Martin Brandl, der mir mit Rat und Tat zur Seite gestanden hat, und all meinen Kollegen des Zentrums für Integrierte Sensorsysteme an der Donau Universität Krems, die mir oft hilfreiche Tipps geben konnten.

Ich möchte mich auch bei meiner Schwester und meinen Eltern, die immer für mich da sind, und bei meinem besten Freund Patrick, der mich oft nach stressigen Arbeits- oder Studiumstagen zum Lachen bringen konnte, bedanken.

Mein größter Dank gilt meinem Freund Andreas, der mich immer beim Lernen unterstützt, meine Launen ertragen und mir Mut gemacht hat, wenn ich nicht weiter wusste. Danke, dass du mir Durchhaltevermögen und Lebensfreude auch an schwierigen Tagen geschenkt hast!

Diese Arbeit wurde ihm Rahmen des Projekts „Microwave based biosensors with printable surface modifications for point-of-care testing of haemodialysis patients“ verfasst und von der NÖ Forschungs- und Bildungsges.m.b.H. (NFB) durch den Life Science Call LS13-023 unterstützt.

ABSTRACT

This thesis is about split-ring resonators and their application as biosensors. Split ring resonators are a special resonator type which consists of a metallic loop etched on a dielectric substrate. They provide a resonant frequency which is determined by the electromagnetic parameters of the substrate and the geometry of the metallic loop. For sensor applications, the metallic surface will be bio-functionalized and if molecules are attaching onto the resonator surface the resonant frequency of the resonator is changed proportional to the load of biomolecules.

The aim of the thesis is to optimize the design of different split-ring resonators to get a high-quality biosensor. The operating frequency of the investigated split-ring resonators is between 1.5 and 2.5GHz.

First, split-ring resonators are theoretically described and the underlying physics is explained. Then a model of split-ring resonators was designed using the microwave simulation tool HFSS. HFSS is a high-frequency simulation software which offers all functions that are necessary for the simulation of split-ring resonators in the microwave regime, like definition of materials with frequency-dependent electromagnetic properties, calculation of scattering parameters and simulation of the electric field. The model was validated by comparing the frequency-dependent scattering parameters of the split-ring resonators measured with a network analyzer with the results of the computation using basics statistics. Having a valid model, the geometry of the split-ring resonator was optimized in order to obtain high resonator sensitivity. The sensitivity is an indicator for the ability of a sensor to react to small changes, in our case the binding of biomolecules. The sensitivity of the sensor depends on the geometry of the metallic loop and the relative permittivity of the dielectric substrate. In this work, the influence of the geometric parameters will be regarded. The sensitivity increases with the quality factor of the resonator, which represents the ratio of the stored energy in the resonator to the energy loss. Therefore the quality factor should be highest possible to get a high-sensitive biosensor. Different structures are looked at, and as a result the interdigital centered-gap split-ring resonator, which is a split-ring resonator with slightly modified geometry, is found to provide the highest quality factor.

The interdigital centered-gap split-ring resonator was analyzed carefully. Buffer solutions are put at the area where the resonator is the most sensitive for changes in permittivity. In

order to do this, the electric field was simulated in HFSS. At the interdigital structure, a maximum of the electric field amplitude was found. Different parts of the interdigital structure are covered with a buffer solution. As a consequence, an area for the buffer solution was found at which the frequency shift is about 30MHz.

KURZFASSUNG

Das Thema dieser Arbeit sind Split-Ring Resonatoren und ihre Anwendung als Biosensoren. Split-Ring Resonatoren sind spezielle Arten von Resonatoren, die aus einem metallischen Ring oder rechteckförmiger Schleife auf einem dielektrischen Substrat bestehen. Diese Resonatoren haben eine Resonanzfrequenz, die durch die elektromagnetischen Parametern des Substrats und die Geometrie der Schleife bestimmt ist. Für ihre Anwendung als Sensor werden die metallischen Oberflächen bio-funktionalisiert. Wenn nun Moleküle an die Oberfläche binden, ändert sich die Eigenfrequenz des Resonators proportional zur Konzentration der gebundenen Moleküle an der Oberfläche.

Ziel dieser Arbeit ist es, die Struktur verschiedener Split-Ring Resonatoren zu optimieren um einen hochqualitativen Biosensor zu erhalten. Die Resonanzfrequenzen der betrachteten Resonatoren liegen zwischen 1.5 und 2.5GHz.

Zu Beginn werden Split-Ring Resonatoren und die zugrundeliegende physikalische Theorie erklärt. Anschließend wurde ein Simulationsmodell eines Split-Ring Resonators erstellt. Dies geschieht mit der Simulations-Software HFSS, die im Bereich der Mikrowellen operiert. HFSS ist eine Hochfrequenz-Simulationssoftware, die alle Funktionen bietet, die zur Simulation von Split-Ring Resonatoren im Mikrowellenbereich notwendig sind, zum Beispiel die Definition von Materialien mit frequenzabhängigen elektromagnetischen Eigenschaften, die Berechnung von Streuparametern und die Simulation der elektrischen Felder. Um das Modell zu verifizieren, wurden die frequenzabhängigen Streu-Parameter des Split-Ring Resonators mit einem Netzwerk-Analysator gemessen und mit den Simulationsergebnissen verglichen. Nach der Validierung des Modells wurde die Geometrie des Split-Ring Resonators optimiert, um hohe Sensitivität zu erreichen. Die Sensitivität ist ein Indikator für die Fähigkeit eines Sensors, auf kleine Änderungen zu reagieren, was in unserem Fall die Anbindung von Biomolekülen ist. Die Sensitivität des Sensors hängt von der Geometrie der metallischen Schleife und der relativen Permittivität des dielektrischen Substrats ab. In dieser Arbeit wird der Einfluss der geometrischen Parameter untersucht. Die Sensitivität steigt mit steigender Resonatorgüte, die das Verhältnis der im Resonator gespeicherten Energie zum Energieverlust darstellt. Um einen hochsensitiven Biosensor zu erhalten, sollte die Güte daher höchstmöglich sein. Verschiedene Strukturen wurden untersucht, mit dem Ergebnis,

dass der *interdigital centered-gap Split-Ring Resonator*, ein Split-Ring Resonator mit leicht veränderter Geometrie, die höchste Resonatorgüte bietet.

Der *interdigital centered-gap Split-Ring Resonator* wurde weiter untersucht. Pufferlösungen werden an den Teil des Resonators aufgebracht, der am sensitivsten auf Permittivitätsänderungen reagiert. Um diesen Teil zu finden, wurde das elektrische Feld in HFSS simuliert. Bei der interdigitalen Struktur befindet sich das Maximum der elektrischen Feldamplitude. Verschiedene Stellen dieser Struktur werden mit einer Pufferlösung bedeckt. Am Ende wurde eine Stelle gefunden, an der die Frequenzänderung etwa 30MHz beträgt.

SYMBOLS

$a_i, \quad i,j \in \{1,2\}$	Incident wave quantity	$[\sqrt{\mathrm{W}}]$
$b_i, \quad i,j \in \{1,2\}$	Reflected wave quantity	$[\sqrt{\mathrm{W}}]$
$\boldsymbol{B}$	Magnetic flux density	[T]
c	Speed of light in free space	$[\mathrm{m/s}]$
C	Capacitance	[F]
$\boldsymbol{D}$	Electric flux density	$[\mathrm{As} \,/\, \mathrm{m}^2]$
$\boldsymbol{E}$	Electric field	$[\mathrm{V/m}]$
f	Frequency	[Hz]
$\boldsymbol{H}$	Magnetic field	$[\mathrm{A/m}]$
I	Electric current	[A]
$\boldsymbol{J}$	Electric current density	$[\mathrm{A} \,/\, \mathrm{m}^2]$
k	Wave number	
L	Inductance	[H]
n	Refractive index	
Q	Electric charge	[C]
Q_f	Quality factor	
R	Resistance	[Ω]
$S_{ij}, \quad i,j \in \{1,2\}$	S-parameter	
U	Voltage	[V]
v_p	Phase velocity of an electromagnetic wave in given medium	$[\mathrm{m/s}]$
W	Energy	[J]
X	Reactance	[Ω]
Z	Electrical impedance	[Ω]
Z_p	Wave impedance	[Ω]

δ	Dielectric function	
$\tan \delta_L$	Loss tangent	
ε	Electric permittivity	$[\mathrm{F/m}]$
$\varepsilon_r' \,/\, \varepsilon_r''$	Real/imaginary part of complex permittivity	
ε_r	Relative permittivity	
μ	Magnetic permeability	$[\mathrm{H/m}]$
μ_r	Relative permeability	

ρ	Electric charge density	$[\mathrm{C} / \mathrm{m}^3]$
σ	Electric conductivity	$[\mathrm{S/m}]$
ω	Angular frequency	$[1/s]$

Inhaltsverzeichnis

1. INTRODUCTION

Nowadays, the development of sensor devices makes up a huge field in different research areas. Important topics are for example the development of biosensors for biomedical applications like diagnostics or disease monitoring, environmental monitoring like the detection of toxic agents or bacteria in drinking water, homeland security or environmental monitoring [1]. For the detection of biomolecules a wide range of approaches exist. Different methods, like micro-cantilevers [2], surface plasmon resonance [3, 4] and nanowire-based biosensors [5] have been developed. Although all these biosensing methods, regardless whether based on mechanical, electrical, or optical transducers, feature highly sensitive, real-time, and label-free detection, most of them still require sophisticated and complex fabrication processes or expensive instrumentation for read-out [6]. A concept that has been attempted only very recently exploits evanescent waves in the microwave regime, which offers the advantage of low-cost sender and receiver components. In particular, microwave-resonator based designs such as split-ring resonators (SRRs) are considered to be highly promising transducers for the detection of biomolecules in point-of-care applications because of their simpler handling and multiplexing capability [6].

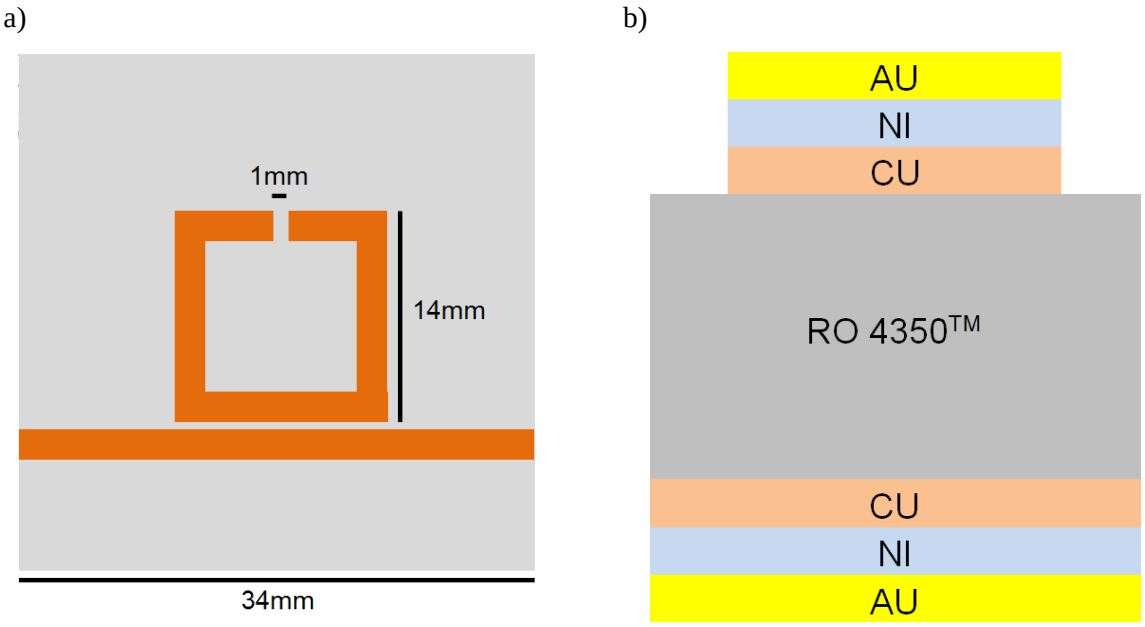

Figure 1: Basic structure of a split-ring resonator. a) Geometry, dimensions are an example for a resonator operating in the microwave regime. b) Layer structure, copper-nickel-gold composition (35µm-5µm-0.1µm) on a Rogers 4350B™ high frequency laminate with a relative permittivity ε_r of 3.66 and a dielectric loss tangent of 0.0031.

The basic structure of such a biosensor operating in the microwave regime is shown in Figure 1a). It consists of a microstrip line and a metallic loop etched on a dielectric substrate. Figure 1b) shows the layer structure of the SRR biosensor investigated in this thesis. The metallic ground plane and the metallic loop consist of a three-layer composite of copper, nickel and gold (35µm-5µm-0.1µm), respectively. The used dielectric substrate is a Rogers 4350B^{TM} high frequency laminate with a relative permittivity ε_r of 3.66 and a dielectric loss tangent of 0.0031. This substrate is chosen because it offers low relative permittivity and low losses in the microwave range which leads to higher sensitivity [7]. The SRR offers a resonant frequency that is determined by the relative permittivity of the substrate and the geometry of the loop. For sensing applications parts of the metallic loop will be bio-functionalized so that biomolecules can bind. The binding of the molecules leads to a change in permittivity. As a result, the resonant frequency shifts proportional to the load of biomolecules [8].

In this work, a microwave biosensor with a high quality factor will be developed. Chapter 2 provides an overview to the theory needed to understand the physical background of the work. The Maxwell's equations and the material equations will be explained. The homogeneous Helmholtz equation for the time harmonic electric field and the wave equation for the electric field will be derived. Resonators and their basic functionality will be mentioned shortly. Then the sensor principle will be explained.

In the next chapter, a simple split-ring resonator will be introduced and a model will be built in the high-frequency simulation software HFSS. The model will be validated by comparing the results with measurements using basic statistics. Afterwards, the geometry of the split-ring resonator will be improved to in terms of the quality factor to ensure high sensitivity. The sensitivity of the biosensor is a measure for the ability of a sensor to react to small changes [7]. By increasing the quality factor of the resonator, the sensitivity gets higher [9]. The quality factor depends on the geometry of the metallic loop and on the used dielectric substrate.

In chapter 4, more complex geometries will be introduced. Their performance in terms of their quality factor will be compared and the different geometries will be improved to get a higher quality factor using Finite Element Simulations (FEM). Moreover, an equivalent circuit will be developed and adjusted to the developed biosensor using electronic design automation software.

To analyze the response of the developed biosensor device to different solutions, the electromagnetic properties of different buffer solutions will be determined using the ‘Principle of Reflection Method’. The method is described in [10] and is slightly altered to fit our requirements as described in chapter 5. Having characterized the buffer solutions in terms of their electric permittivity and conductivity, further simulations can be performed with additional buffer droplets on the sensitive area of the biosensor device. Different positions of the droplets will be regarded to find a position with detectable frequency shift.

In the last chapter, the results will be summarized and discussed.

2. INITIATORY THEORY

In this section, basics of electrical engineering will be explained. Important terms are defined and Maxwell's Equations are shown. Then the linkage between the theory and the working principle of the microwave biosensor will be established.

2.1. PHYSICAL QUANTITIES

MAXWELL'S EQUATIONS

The basis of classical electrodynamics is formed by Maxwell's equations [11]. Based on these equations, all principles of electromagnetic fields and waves can be derived.

$$\vec{\nabla} \times \boldsymbol{H} = \boldsymbol{J} + \frac{\partial \boldsymbol{D}}{\partial t} \quad (1)$$

$$\vec{\nabla} \times \boldsymbol{E} = -\frac{\partial \boldsymbol{B}}{\partial t} \quad (2)$$

$$\vec{\nabla} \cdot \boldsymbol{B} = 0 \quad (3)$$

$$\vec{\nabla} \cdot \boldsymbol{D} = \rho \quad (4)$$

$\boldsymbol{H}$ is the magnetic field, $\boldsymbol{J}$ the electric current density, $\boldsymbol{D}$ is the electric flux density, $\boldsymbol{E}$ is the electric field, $\boldsymbol{B}$ is the magnetic flux density and ρ is the electric charge density. Variables in bold print denote vector quantities. Equations (1) and (2) are vector equations; equations (3) and (4) are scalar equations. This results in eight equations for sixteen quantities. In the next section, the so-called material equations will be introduced. They make up three additional vector equations for the sixteen quantities.

The physical meaning of the equations is the following: equation (1) shows that electric currents lead to magnetic eddy current fields. Changes in magnetic flux density cause electric eddy current fields. This relationship is shown by equation (2). Magnetic fields are source-free (equation (3)) and electric fields are source fields caused by electric charge (equation (4)).

MATERIAL EQUATIONS

The material equations describe the dependencies of the electric/magnetic flux densities to the electric/magnetic fields and the dependency of the electric current density on the electric field. In a linear isotropic medium, we get following equations [12]:

$$\boldsymbol{D} = \varepsilon \boldsymbol{E} \tag{5}$$

$$\boldsymbol{B} = \mu \boldsymbol{H} \tag{6}$$

$$\boldsymbol{J} = \sigma \boldsymbol{E} \tag{7}$$

Equation (7) is Ohm's law. ε is electric permittivity, μ denotes magnetic permeability and σ is electric conductivity. Electric permittivity and permeability will be further discussed in the next section.

ELECTRIC PERMITTIVITY AND PERMEABILITY

The electric permittivity $\varepsilon = \varepsilon_r \varepsilon_0$ and permeability $\mu = \mu_r \, \mu_0$ describe the coupling of a material to the electric and magnetic field components of an electromagnetic wave [13].

In literature, relative permittivity ε_r and relative permeability μ_r are frequently mentioned. Relative permittivity ε_r is the ratio of permittivity ε to vacuum permittivity ε_0 and relative permeability μ_r is the ratio of permeability μ to vacuum permeability μ_0. The vacuum permittivity ε_0 and vacuum permeability μ_0 in SI units are $\varepsilon_0 = 8.85 \cdot 10^{-12}$F/m and $\mu_0 = 4\pi \cdot 10^{-7}$H/m [13]. These quantities are related to speed of light in the vacuum c, the refractive index n, the phase velocity v_p of an electromagnetic wave in a given medium and the wave impedance Z_w as follows [11], [13]:

$$c = \sqrt{\frac{1}{\varepsilon_0 \mu_0}} \tag{8}$$

$$n = \frac{c}{v_p} = \sqrt{\varepsilon_r \mu_r} \tag{9}$$

$$Z_w = \sqrt{\frac{\mu}{\varepsilon}} \tag{10}$$

Another important term is the complex permittivity. It is defined as:

$$\varepsilon_r = \varepsilon_r' - i\varepsilon_r'' \tag{11}$$

ε_r' and ε_r'' are the real and imaginary part of complex permittivity, respectively. The magnitude of the complex permittivity can be calculated using (12):

$$|\varepsilon_r| = \sqrt{\varepsilon_r'^2 + \varepsilon_r''^2} \tag{12}$$

ELECTRIC CONDUCTIVITY

Electric conductivity σ is defined by the linear relationship in Ohm's Law which is shown in equation (7). It is linked to the imaginary part of complex permittivity via following relationship [14] with f denoting the frequency:

$$\sigma = 2\pi f \varepsilon_r'' \varepsilon_0 \tag{13}$$

CAPACITORS

The following sections use the theory described in [15]. Basically, capacitors consist of two insulated electrodes placed on the opposite of each other. Between these electrodes, a dielectric material is placed. Having a potential difference between the two electrodes, the capacitor stores the energy W in its electric field and takes up the electric charge Q. Following formulas describe the relationships between the voltage U caused by the potential difference, the stored energy W, and the electric charge Q:

$$W = \frac{1}{2} C U^2 \tag{14}$$

$$Q = CU \tag{15}$$

For lossless capacitors, following relationship between electric charge Q, voltage U, current I and capacitance C can be observed:

$$I = \frac{dQ}{dt} = C\frac{dU}{dt} \tag{16}$$

$$U = \frac{1}{C}\int I\, dt \tag{17}$$

The proportionality factor C is called capacitance. It depends on the structure and sizes of the capacitor and the dielectric material. For the simple example of a parallel-plate capacitor, like it is shown in Figure 2a) based on [15], the capacitance can be calculated with following formula:

$$C = \frac{\varepsilon_0 \varepsilon_r A}{d} \tag{18}$$

It increases with increasing plate area A and decreasing distance d. ε_r is the relative permittivity of the dielectric between the metallic plates.

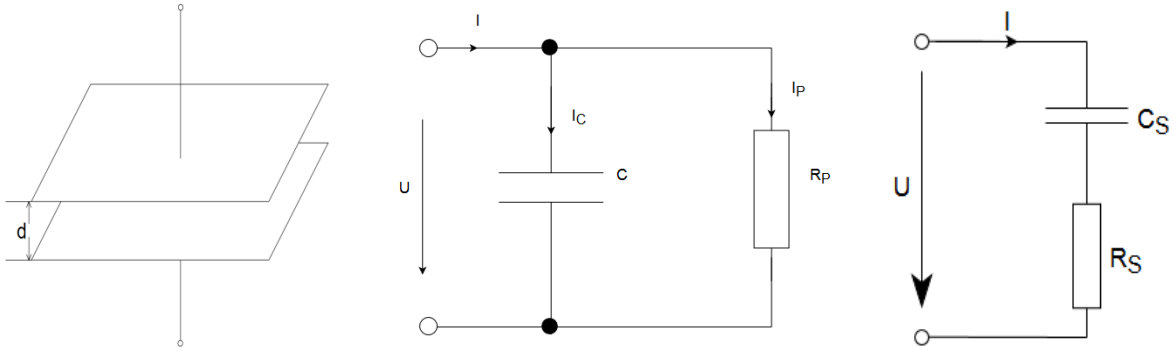

a) b) c)

Figure 2: a) Parallel-Plate capacitor with plate area A, distance d and filled with dielectric with relative permittivity ε_r, b) Parallel circuit with voltage U, current I, capacitive current I_C, leakage current I_P, capacitance C and loss resistance R_P, c) Series circuit with voltage U, current I, series capacitance C_S, series resistance R_S.

DIELECTRIC LOSS

Since electrodes can't be perfectly insulated and the polarization of the dielectric changes, for real capacitors the current is shifted from the 90°- position with the loss angle δ_L. The equivalent circuit of a real lossy capacitor is shown in Figure 2b). The loss tangent is defined to be the tangent of the loss angle δ_L. It is the ratio of capacitive reactance $X_C = \frac{1}{\omega C}$ to loss resistance R_p:

$$\tan \delta_L = \frac{X_C}{R_p} = \frac{1}{\omega C R_p} \tag{19}$$

The relationship between loss tangent, electric conductivity and complex permittivity is the following:

$$\tan \delta_L = \frac{\sigma}{2\pi f \varepsilon_0 \varepsilon_r'} = \frac{\varepsilon_r''}{\varepsilon_r'} \tag{20}$$

QUALITY OF CAPACITORS

The inverse of the loss tangent is defined to be the quality factor (Q-factor) Q_f of the capacitor.

$$Q_f = \frac{1}{\tan \delta_L} \tag{21}$$

If the Q-factor is high enough, which simultaneously means that the loss tangent is low, the equivalent circuit of the capacitor can be assumed to be a series circuit like it is displayed in Figure 2c). In this case, the loss tangent can be calculated using following formula:

$$\tan \delta_L = \frac{R_s}{X_s} = R_s \omega C \tag{22}$$

THE ELECTRIC FIELD

Since the electric field strength as a function of place is a vector, the electric field $\boldsymbol{E}$ has to be a vector field [16]. Therefore it has a magnitude and a direction. Vector fields can be illustrated by using field lines. Electric field lines are tangent to the vectors of electric field strength. The electric field is a source field, caused by electric charge Q. This relation is shown by equation (4).

To get a better understanding of electric fields, the simplest example of an electric field caused by a point charge Q_p will be explained. In this case, the electric field is radially symmetric and it can be calculated using the Coulomb formula, with r denoting the distance to the charge and $\boldsymbol{e}_r$ the unit vector of the position vector [16]:

$$\boldsymbol{E}(\boldsymbol{r}) = \frac{Q_p}{4\pi\varepsilon_0 r^2} \boldsymbol{e}_r \tag{23}$$

The magnitude of the electric field decreases with increasing r^2. Having n charges Q_i placed at positions $\boldsymbol{r}_i$, we can use the superposition principle to calculate the electric field in dependency on position vector $\boldsymbol{r}$ [11]:

$$\boldsymbol{E}(r) = \sum_{i=1}^{n} \frac{Q_i}{4\pi\varepsilon_0} \frac{(\boldsymbol{r} - \boldsymbol{r}_i)}{|\boldsymbol{r} - \boldsymbol{r}_i|^3} \tag{24}$$

Regarding more complex situations, the electric field can be calculated using the Maxwell equations.

WAVE EQUATION AND HELMHOLTZ EQUATION

One of the fundamental natures of Maxwell's equations is that their solutions are propagating waves which transfer energy through matter or space.

Partial differential equations such as the Maxwell equations (1) and (2) can be solved by using the method of separations of variables [17]. First some mathematical conversions in equation (2) are necessary:

$$\nabla \times \nabla \times \boldsymbol{E} = -\nabla \times \frac{\partial \boldsymbol{B}}{\partial t} \tag{25}$$

With equations (6), (1) and (7) we get:

$$\begin{aligned} \nabla \times \nabla \times \boldsymbol{E} &= -\mu \left(\nabla \times \frac{\partial \boldsymbol{H}}{\partial t} \right) \\ &= -\mu \frac{\partial}{\partial t} (\nabla \times \boldsymbol{H}) \\ &= -\mu \frac{\partial}{\partial t} \left(\boldsymbol{J} + \varepsilon \frac{\partial \boldsymbol{E}}{\partial t} \right) \\ &= -\mu \frac{\partial}{\partial t} \left(\sigma \boldsymbol{E} + \varepsilon \frac{\partial \boldsymbol{E}}{\partial t} \right) \end{aligned} \tag{26}$$

Following relationship can be verified using simple mathematics and will be applied to the last equation:

$$\nabla \times \nabla \times \boldsymbol{A} = \nabla \nabla \cdot \mathbf{A} - \Delta \boldsymbol{A} \tag{27}$$

Subsequently we get:

$$\nabla \nabla \cdot \mathbf{E} - \Delta \boldsymbol{E} = -\mu \frac{\partial}{\partial t} \left(\sigma \boldsymbol{E} + \varepsilon \frac{\partial \boldsymbol{E}}{\partial t} \right) \tag{28}$$

And with equations (4) and (5) we get the wave equation for the electric field $\boldsymbol{E}$ [11]:

$$\Delta \boldsymbol{E} = \mu\sigma \frac{\partial \boldsymbol{E}}{\partial t} + \mu\varepsilon \frac{\partial^2 \boldsymbol{E}}{\partial t^2} + \nabla \frac{\rho}{\varepsilon} \tag{29}$$

Considering an insulating material which is free of charges ($\rho = 0$), we get the more specific wave equation which is valid for technical dielectrics:

$$\Delta \boldsymbol{E} = \mu\varepsilon \frac{\partial^2 \boldsymbol{E}}{\partial t^2} \tag{30}$$

In the special case of a homogeneous material and a time harmonic electric field, we get the homogeneous Helmholtz equation for the time harmonic electric field $\boldsymbol{E}$ from equation (29):

$$\Delta \boldsymbol{E} + \omega^2 \mu \left(\varepsilon - i\frac{\sigma}{\omega}\right)\boldsymbol{E} = 0 \tag{31}$$

The term in brackets is defined to be the dielectric function $\delta \coloneqq \varepsilon - i\frac{\sigma}{\omega}$ and ω denotes the angular frequency $\omega = 2\pi f$.

WAVE NUMBER

The wave number k can be derived by solving equation (31) using the method of separation of variables. This is by inserting the ansatz $E_n(x,y,z) = X_n(x) \cdot Y_n(y) \cdot Z_n(z)$ for $n \in \{1,2,3\}$ into equation (31). This leads to following equation which is true for all $n \in \{1,2,3\}$:

$$\begin{aligned}
0 &= \Delta E_n + \omega^2 \mu \delta E_n \\
&= \frac{\partial^2 E_n}{\partial x^2} + \frac{\partial^2 E_n}{\partial y^2} + \frac{\partial^2 E_n}{\partial z^2} + \omega^2 \mu \delta E_n \\
&= \frac{\partial^2 X_n(x) \cdot Y_n(y) \cdot Z_n(z)}{\partial x^2} + \frac{\partial^2 X_n(x) \cdot Y_n(y) \cdot Z_n(z)}{\partial y^2} \\
&\qquad + \frac{\partial^2 X_n(x) \cdot Y_n(y) \cdot Z_n(z)}{\partial z^2} + \omega^2 \mu \delta X_n(x) \cdot Y_n(y) \cdot Z_n(z) \\
&= Y_n(y) \cdot Z_n(z) \frac{\partial^2 X_n(x)}{\partial x^2} + X_n(x) \cdot Z_n(z) \frac{\partial^2 Y_n(y)}{\partial y^2} + X_n(x) \cdot Y_n(y) \cdot \frac{\partial^2 Z_n(z)}{\partial z^2} \\
&\qquad + \omega^2 \mu \delta X_n(x) \cdot Y_n(y) \cdot Z_n(z) \\
&= \frac{1}{X_n(x)} \frac{\partial^2 X_n(x)}{\partial x^2} + \frac{1}{Y_n(y)} \frac{\partial^2 Y_n(y)}{\partial y^2} + \frac{1}{Z_n(z)} \frac{\partial^2 Z_n(z)}{\partial z^2} + \omega^2 \mu \delta
\end{aligned} \tag{32}$$

The resulting differential equation is the following, with k denoting the wave number:

$$\frac{1}{X_n(x)} \frac{\partial^2 X_n(x)}{\partial x^2} + \frac{1}{Y_n(y)} \frac{\partial^2 Y_n(y)}{\partial y^2} + \frac{1}{Z_n(z)} \frac{\partial^2 Z_n(z)}{\partial z^2} = -\omega^2 \mu \delta =: -k^2 \tag{33}$$

Each summand depends only on one specific variable, and there are not more than one summand depending on the same variable. As a result, the equation is valid if and only if the summands are constant. This leads to nine ordinary differential equations of second order:

$$\frac{1}{X_n(x)} \frac{d^2 X_n(x)}{dx^2} = -k_{X_n}^2 \qquad n \in \{1,2,3\} \tag{34}$$

$$\frac{1}{Y_n(y)} \frac{d^2 Y_n(y)}{dy^2} = -k_{Y_n}^2 \qquad n \in \{1,2,3\} \tag{35}$$

$$\frac{1}{Z_n(z)}\frac{d^2Z_n(z)}{dz^2} = -k_{Z_n}^2 \qquad n \in \{1,2,3\} \tag{36}$$

In equations (34)-(36), the variables k_{X_n}, k_{Y_n} and k_{Z_n} denote the separation constants for which equation (33) is true. These constants need to fulfill following relationship:

$$k_{X_n}^2 + k_{Y_n}^2 + k_{Z_n}^2 = k^2 = \omega^2\mu\delta \qquad n \in \{1,2,3\} \tag{37}$$

This leads to the general solutions:

$$X_n(x) = e^{-ik_{X_n}x} \qquad n \in \{1,2,3\} \tag{38}$$

$$Y_n(x) = e^{-ik_{Y_n}y} \qquad n \in \{1,2,3\} \tag{39}$$

$$Z_n(x) = e^{-ik_{Z_n}z} \qquad n \in \{1,2,3\} \tag{40}$$

This solution of the expression for the time harmonic electric field E at point $\mathrm{P} = \begin{pmatrix} \mathrm{x} \\ \mathrm{y} \\ \mathrm{z} \end{pmatrix}$ and time t in homogeneous material is a spherical wave:

$$E(x,y,z,t) = \begin{pmatrix} e^{-i(k_{X_1}x + k_{Y_1}y + k_{Z_1}z - \omega t)} \\ e^{-i(k_{X_2}x + k_{Y_2}y + k_{Z_2}z - \omega t)} \\ e^{-i(k_{X_3}x + k_3 y + k_{Z_3}z - \omega t)} \end{pmatrix} \tag{41}$$

The wave number k corresponds to the number of waves per unit distance.

DISPERSION

All relationships in this part are taken from [11]. In free space, the wave number k equals $\omega\sqrt{\mu_0\varepsilon_0}$ because there is no conductivity ($\sigma = 0$). This results in following relationship, with c denoting the speed of light in free space:

$$k = \frac{\omega}{c}. \tag{42}$$

In a non-conducting dielectric free of charges, the wave number k equals $\omega\sqrt{\mu\varepsilon}$ because $\sigma = 0$. Combining this relation with equation (9), the dispersion relation for plane electromagnetic waves in an ideal insulator is obtained:

$$k = \frac{\omega}{v_p} \tag{43}$$

v_p denotes the phase velocity of the electromagnetic wave in the given medium with $v_p = 1/\sqrt{\varepsilon\mu}$. It is defined to be the propagation velocity of the phase of the wave in the

medium. In general, the dispersion relation is the dependency of the wave number k on the angular frequency ω:

$$k = k(\omega) \tag{44}$$

Dispersion is referred to the fact that the phase velocity can be a function of frequency. In general, following relationship is known:

$$k(\omega) = \frac{\omega}{v_p} = \frac{\omega}{c}\sqrt{\varepsilon\mu} = \frac{\omega}{c}n \tag{45}$$

SCATTERING PARAMETERS

In high-frequency engineering, scattering parameters, also named S-parameters, serve to describe properties of circuits without using voltage and current. They are calculated via the incident and reflected waves at the ports of the circuit [18]. The used wave quantities a_i and b_i can be calculated using the incident and reflected voltages U_{pi} and $U_{ri}, i \in \{1,2\}$ and the wave impedance Z_{Li}, with a_i denoting the transmitted wave at port i and b_i denoting the received wave at port i:

$$a_i = \frac{U_{pi}}{\sqrt{\mathrm{Re}(Z_{Li})}} \qquad i \in \{1,2\} \tag{46}$$

$$b_i = \frac{U_{ri}}{\sqrt{\mathrm{Re}(Z_{Li})}} \qquad i \in \{1,2\} \tag{47}$$

In a two-port network, compare Figure 3 based on [18], following formulas can be used to calculate the S-parameters:

$$S_{11} = \left.\frac{b_1}{a_1}\right|_{a_2=0} \tag{48}$$

$$S_{12} = \left.\frac{b_1}{a_2}\right|_{a_1=0} \tag{49}$$

$$S_{21} = \left.\frac{b_2}{a_1}\right|_{a_2=0} \tag{50}$$

$$S_{22} = \left.\frac{b_2}{a_2}\right|_{a_1=0} \tag{51}$$

S_{11} denotes the input reflection coefficient, S_{12} denotes the reverse transmission coefficient, S_{21} is the forward transmission coefficient and S_{22} is the output reflection

coefficient [19]. In this work, the logarithmic S-parameters will be used, with log denoting the decadic logarithm:

$$S_{ij}\,[dB] = 10\log\left|S_{ij}\right|^2 \qquad (52)$$

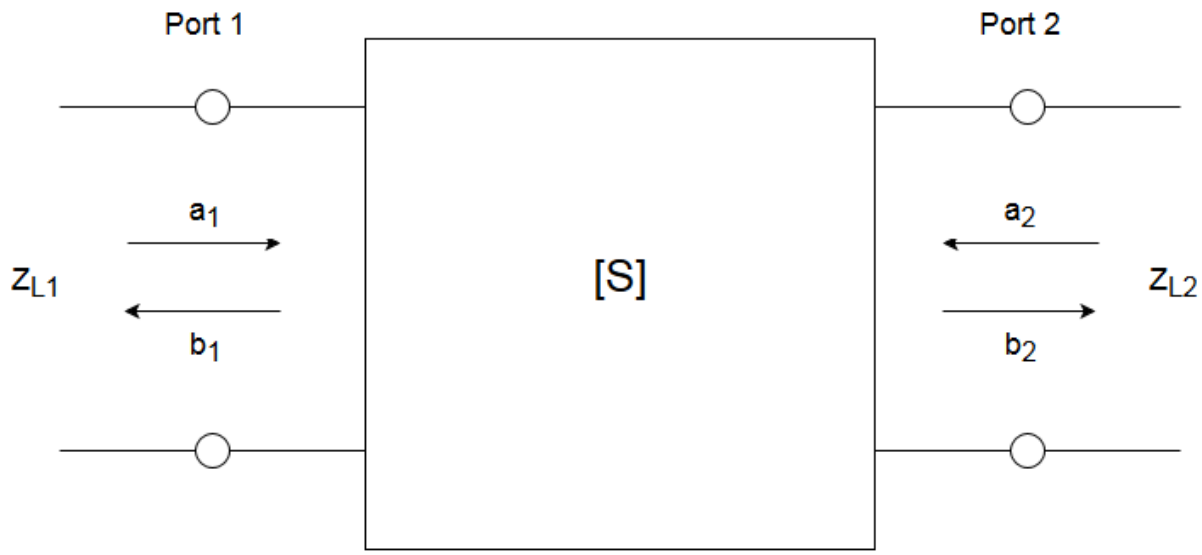

Figure 3: Two-port network with transmitted waves a_i, received waves b_i, wave impedance Z_{Li} and scattering matrix S.

2.2. Parts Of the Biosensor

Resonator

Resonators are passive devices. The coupling of a coil to a capacitor forms a resonant circuit [15]. Both coil and capacitor have the ability to store energy. A capacitor stores energy in form of the electric field depending on the voltage and a coil stores energy in form of a magnetic field depending on the current. If at least one of those elements contains energy, compensatory current flow will arise and due to an effective resistance R_s the stored energy is converted into heat. Since this electric circuit consists of a resistor, an inductor and a capacitor, it is denoted as RLC circuit. Figure 4 based on [15] shows the equivalent circuit of a simple resonator:

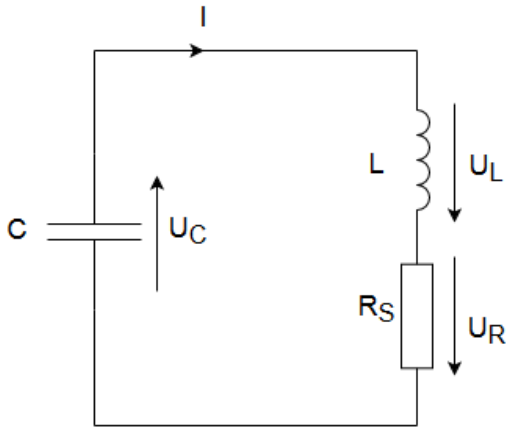

Figure 4: Resonant circuit with capacitance C, inductance L and effective resistance R_s.

Assuming that there is no effective resistance, the circuit will oscillate undamped with the resonant frequency f_0:

$$f_0 = \frac{1}{2\pi\sqrt{LC}} \tag{53}$$

The impedance Z of an RLC circuit can be calculated using following fomula with X denoting reactance and R denoting resistance [15]:

$$Z = R + iX = R + i\left(\omega L - \frac{1}{\omega C}\right) \tag{54}$$

At resonance, $\omega = \omega_0 = 1/\sqrt{LC}$, the imaginary part of the impedance becomes zero ($X = 0$). For other frequencies ω the circuit is inductive in case of a positive reactance, and the circuit is capacitive in case of a negative reactance.

Split-Ring Resonator

Split-ring resonators are a special type of resonator. Basically, they consist of a metallic open loop with a dielectric gap, compare Figure 5. At resonance, a strong current oscillation in the metallic loop occurs and a localized electric field in the gap can be observed. This localized electric field is very sensitive to local permittivity changes [20]. Figure 5 from [20] shows the basic structure of a split-ring resonator coupled to a microstrip line and its equivalent circuit consisting of an RLC-circuit coupled via mutual inductance to the microstrip inductance.

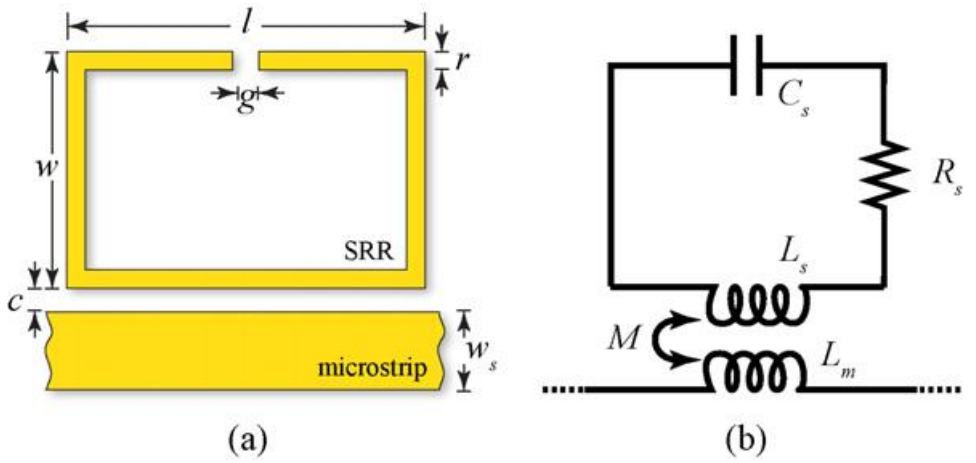

Figure 5: Basic structure of a split-ring resonator. a) Geometry of the metallic loop coupled to a microstrip line. b) Equivalent circuit with L_m... inductance of the microstrip line, R_s, L_s, C_s as the elements of the resonant loop and M... mutual inductance between the ring and the microstrip line. The figure is taken from [20].

The functionality of this structure is described in [20]: At one end of the microstrip line, a microwave excites the quasi-TEM mode of wave propagation. An oscillating current arises around the strip and a magnetic field circulates around the strip. Due to the magnetic field, a current is induced in the split-ring resonator when the magnetic component is parallel to the axis of the split-ring. When the electric energy stored in the gap of the split-ring equals the magnetic energy stored in the loop, resonance occurs.

According to [20], the impedance of the resonator can be calculated using formula (54) and inserting R_s, L_s and C_s. The capacitance C_s can be approximated using $C_s = C_0 + \varepsilon_{sam} C_c$ where C_0 includes the capacitive effect from the dielectric substrate, the channel walls and the surrounding space. The second summand accounts for the influence of the loaded liquid sample, with C_c denoting the capacitance of an empty channel and ε_{sam} as the complex permittivity of the sample. The total resistance and capacitance R_t and C_t of the resonator are a function of the sample permittivity. The resonant frequency f_0 and the quality factor Q_f of the split-ring resonator can be calculated using following formulas:

$$f_0 = \frac{1}{2\pi\sqrt{L_s C_t}} \tag{55}$$

$$Q_f = \frac{1}{R_t}\sqrt{\frac{L_s}{C_t}} \tag{56}$$

OSCILLATOR

Oscillators are active devices which are used to generate oscillation. The quality of the resonator is the key for the noise in an oscillator [18]. Figure 6 based on figure 6.4 from [18] is an overview of different oscillators showing their quality factor in dependency on the frequency. In this work, we will concentrate on frequencies in the range from 1GHz to 2.5GHz. The chosen resonator is the dielectric resonator DR which offers high quality-factors in the frequency-range of interest.

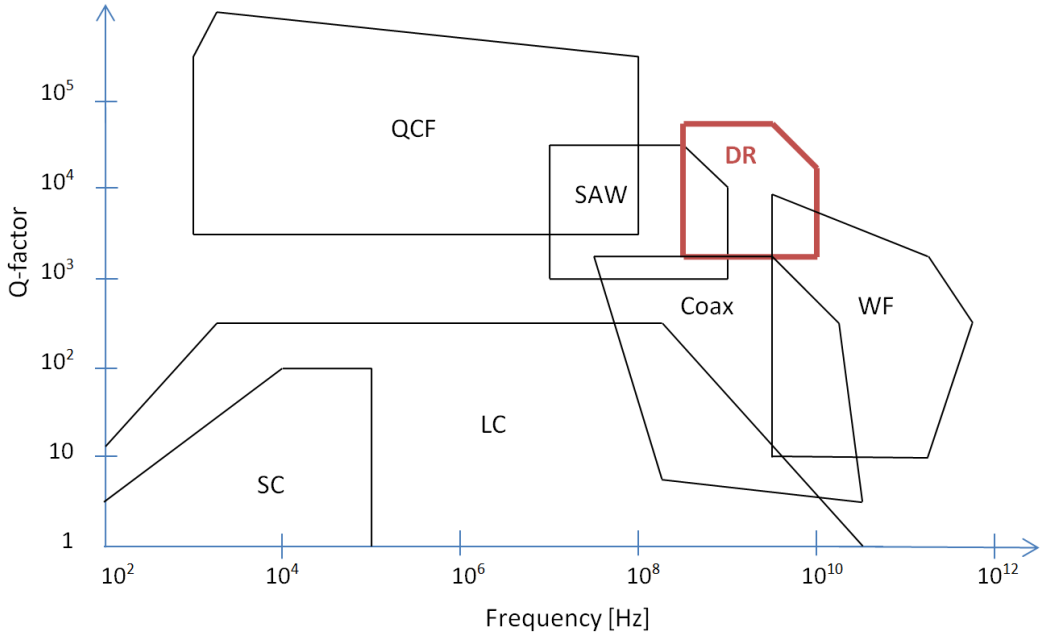

Figure 6: Different types of resonators with high quality factors in different ranges of frequency based on figure 6.4 from [18] (QCF… quartz crystal filter, SC… switched capacitor-filter, LC… LC filter, SAW… surface acoustic waves filter, DR… dielectric resonator filter, Coax… coaxial filter, WF… waveguide filter).

2.3. SENSOR PRINCIPLE

In recent years, high quality microwave resonators came in focus to design devices with unique electromagnetic properties which are not readily occurring in nature. The research group of Pendry [21] was the first who designed a new class of artificial materials with a continuous change of the electric permittivity and the magnetic permeability from positive to negative values. This class of materials is called metamaterials and can produce interesting new effects (e.g. negative refractive index, a perfect microwave cloak and

sophisticated concentrators) which can be used because of their sensitivity for sensing applications.

Guiding of electromagnetic waves on planar surfaces at microwave and optical frequencies has been the subject of some theoretical and experimental study. At the interface of a metallic and a dielectric substrate guided and strong localized modes, so called "surface plasmons", originating from the free electron gas of the metal can be excited. This effect is typically known for optical frequencies but can also be excited in the microwave regime at special designed metallic/dielectric 3D structures [22]. The dielectric function of metals $\varepsilon_m = 1 - \frac{\omega_p^2}{\omega^2}$ results in a negative permittivity ε_m for frequencies below the plasma resonant frequency ω_p of the electron gas. This effect leads to an imaginary refraction index $n_m = \sqrt{\varepsilon_m}$. Therefore, at frequencies below plasma frequency no wave propagation within the metal is possible. Incident electromagnetic waves are totally reflected. Additionally, surface plasmons can exist on the metal-dielectric boundary. If the surface plasmons are excited by an incident electromagnetic field, the reflection coefficient of the metallic surface is reduced because some energy is converted into guided waves and not reflected. At resonance, where the wave vectors of the incident electromagnetic field and the surface plasmon are equal, a maximum of energy is transferred into the surface plasmon resulting in a minimum of reflected light. This effect is very sensitive to permittivity changes on the metallic/dielectric boundary and is well suited for sensor applications.

It was discovered by Pendry et al. [23] that also on periodically structured metallic surfaces, surface plasmons can be excited. The advantage of this technique is that the dispersion characteristics can be controlled by the design and spacing of the holes. Such metallic geometries can also be designed to be metamaterials with negative permeability and permittivity.

In this work, split-ring resonators are used to develop a high-quality microwave biosensor. The basic geometry of this resonator type is shown in Figure 1. These structures combine the best features of microwave-resonators and metamaterials [8]. For sensor applications, small parts of the metallic surface will be bio-functionalized, compare Figure 7. As a result, only specific molecules can bind. The attachment of molecules onto the resonator surface leads to a change of the electric permittivity in proximity of the resonator which results in a shift of the resonant frequency. This shift is proportional to the load of

biomolecules. From this it follows that by measurement of the resonant frequency shift one can determine the concentration of biomolecules.

An advantage of resonant microwave structures for biosensor applications is the small wavelength range in which the resonant interaction occurs. Therefore, it is possible to align several resonant microwave structures with different resonant frequencies along one waveguide. If the distinct resonant sections are coated with different biolayers, with one sensor platform several different biomolecules can be recognized resulting in a multi-functional biosensor.

The sensitivity is an indicator for the ability of a sensor to react to small changes, in our case the binding of biomolecules. According to [7], the sensitivity S of a sensor can be calculated from following formula, with Δl denoting the extension of the electrical length which appears when the split capacity gets positive and $\varepsilon_{r,s}$ denoting the relative permittivity of the sample:

$$S = \frac{\Delta l}{\varepsilon_{r,s}} \tag{57}$$

It depends on the relative permittivity of the substrate, the wave impedance of the resonator structure and the split capacity linked via following relation [7]:

$$\frac{1}{i\omega C} = -iZ_l \cot\left(\frac{\omega \Delta l}{v}\right) \tag{58}$$

with ω denoting angular frequency, Z_l as wave impedance, C as split capacity and v denoting propagation velocity of the electromagnetic wave, $v = \frac{c}{\sqrt{\varepsilon_{eff}}}$.

The biosensor gets more sensitive with increasing extension of the electrical length which can be seen in formula (57). From formula (58) it follows that decreasing effective permittivity ε_{eff} increases Δl. Since effective permittivity can only be decreased by decreasing the relative permittivity of the substrate, a Rogers 4350B™ high frequency laminate is used because it offers a very low relative permittivity of 3.66 and low losses in the frequency range of several GHz. The wave impedance of the resonator structure depends on the width of the split-ring and the split capacity is related to the gap size. Therefore these two parameters will be investigated further to improve the geometry of the biosensor.

SURFACE MODIFICATION

Although the surface modification of the resonator shall not be topic of this work, a short overview of the process will be given in this section. The process is as described in [24, 25]. An overview is given in Figure 7.

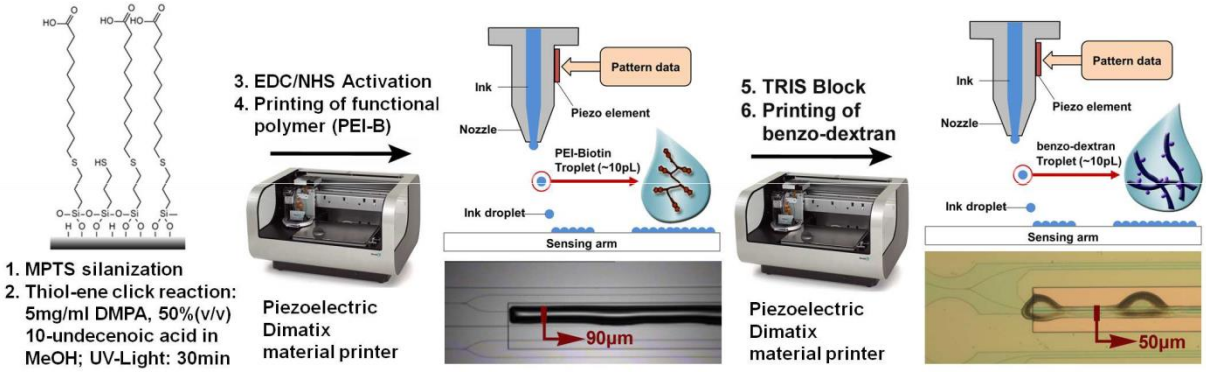

Figure 7: Surface modification of the resonator (figure taken from [24]).

First, the gold surface of the sensor gets silanized using (3-mercaptopropyl)tri-methoxylsilane (MPTMS). This leads to an introduction of thiol-groups. The second step is the modification of the terminal thiols with 10-undecenoic acid using thiol-ene click reaction to obtain a carboxyl-group modified surface [26, 27]. Afterwards, N-hydroxysuccinimidester (NHS) is used in combination with 1-ethyl-3-(3-dimethylamino-propyl)carbodiimides (EDC) for conversion of the surface carboxyl-groups to NHS-esters [28]. These NHS-esters are used in the printing process: amide bonds between amines of the biotin-modified polythylenimine (PEI-B) ink and the surface NHS-esters are formed. In the fifth step, the remaining NHS-esters are blocked with tris(hydroxmethyl)-aminomethan (TRIS). As a last step, benzo-dextran ink is printed and irradiated by UV-light (302nm) which leads to a formation of a dextran hydrogel network (crosslinking). The thickness of the dry hydrogels was determined using surface profilometer measurements [25] and is between 82nm and 126nm. The swelling ratios were obtained using AFM and are between 5 and 10.

After the surface modification process, either antibodies or aptamers can be immobilized on the PEI-B by streptavidin-biotin affinity binding. The antibodies/aptamers function as capture molecules for the biomolecules.

3. DESIGN OF THE SPLIT-RING-RESONATORS

In this section, different designs for split-ring resonators will be discussed. The influence of the gap size and the resonator line width on resonant frequency and Q-factor will be evaluated.

3.1. THE CHOSEN SIMULATION TOOL

HFSS (ANSYS Inc. USA) was chosen to perform the simulations. It is a high-performance full-wave electromagnetic field simulator which employs the Finite Element Method and is used to calculate properties of electromagnetic structures. It is a commercial tool which is widely used e.g. for antenna design.

HFSS offers different solution types. Two of them are used for this work, so they will be described in detail. To calculate the resonant frequencies of the geometry, the *Eigenmode* solution type should be employed. It also allows for calculating different field quantities at the resonant frequencies. A linear equation of following form is solved for sets of $k_0$and $\mathbf{x}$:

$$S\boldsymbol{x} + k_0^2 T\boldsymbol{x} = 0 \tag{59}$$

The matrices S and T depend on the geometry, the materials and the mesh, $\boldsymbol{x}$ is the electric field solution and $k_0$is the free-space wave number. For every electric field solution, one free space wave number corresponding to the mode is found. The corresponding resonant frequency is calculated using:

$$f_0 = \frac{k_0 c}{2\pi} \tag{60}$$

with c denoting the speed of light.

The solution type *Driven Modal* is used to calculate the S-Parameters of passive high-frequency structures (e.g. microstrip lines). Furthermore, the fields are computed. One can choose a specific solution frequency which is used for the convergence and an additional frequency sweep if the fields should be computed at different frequencies.

3.2. SETUP

Before drawing the geometry, one has to set the units for the model. It is recommended that the smallest critical features of the model (e.g. gaps) account for one one-thousandth of the chosen unit. The smallest structures in the model are in the micrometer-range, so the units are chosen to be millimeters. As described in the Online Help of HFSS, the range of dimensions of HFSS is in the range of [1e-6;1e4] times the model units.

The simulation software allows drawing the 3D model in a simple way. For every drawn 3D structure, a material has to be chosen and for 2D structures like rectangles, boundary conditions or excitations can be set. HFSS supports a large material library where new materials can be added and the properties of already defined materials can be changed. Project variables can be defined, which allows easy management of the geometry.

In this work, different geometries will be considered and compared. At first, a geometry will be introduced which has already been manufactured to validate the model.

To make the simulations more realistic, it is important that no unexpected reflections occur at the interface of the geometry and the background. Therefore it is necessary to build an air box around the drawn structure. Different tutorials suggest that the air box should be at least $\lambda/4$ away from the outer surface of the substrate. The resonant frequency of the simulated structure is around 2GHz which yields a wavelength of 150mm. To make sure that the distance to the air box is big enough, the distance is set to 50mm. After drawing the model and setting the materials for the structures, boundary conditions have to be set. The boundaries which are used in the model are the radiation boundary and the perfect electric conductor boundary. The radiation boundary is used for the five faces of the air box which touch the background. It simulates an open problem that allows waves to radiate infinitely far into space, compare HFSS online Help. The perfect electric conductor boundary is assigned to the surface of the structures made of gold. It is an ideal material property with zero resistivity and infinite conductivity.

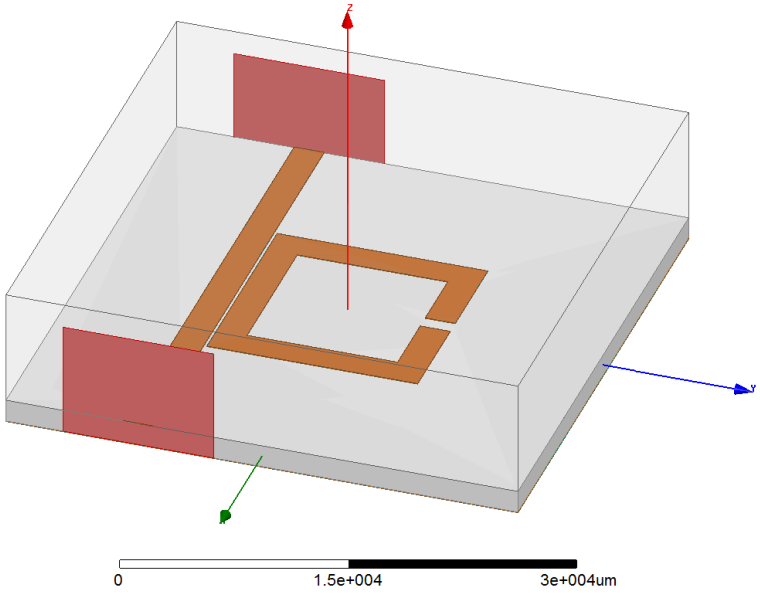

Figure 8: Geometry of the biosensor built in HFSS. The red rectangles are the wave ports; the transparent box is the air box.

The main components of the sensor device are the substrate, the microstrip line, the split-ring resonator, the ground plane and two wave ports. The metallic structures (microstrip line, split-ring resonator and ground plane) consist of a three layer Copper-Nickel-Gold composite with thicknesses of 35µm, 5 µm and 0.1 µm, respectively. The wave ports are modeled as two rectangles like it is shown in Figure 8. As described in the HFSS online Help, the dimensions of the rectangles have to be properly set. It is recommended to set the port height eight times the substrate height and the port width 10 times the width of the microstrip line. The bottom of the rectangles should touch the ground plane.

3.3. SIMPLE GEOMETRY

The first model simulates the simple geometry shown in Figure 1. The width of the microstrip line is 2mm, the distance between the microstrip line and the split-ring is 0.2mm. The height of the dielectric substrate is 1.55mm. After setting up the model, the forward transmission coefficient S_{21} of the split-ring resonator, which is explained in section 2.1 and can be calculated as shown in formula (50), was calculated. The split ring is a square with an outer length of 14mm and a gap of 1mm and a width of 2mm, compare Figure 1.

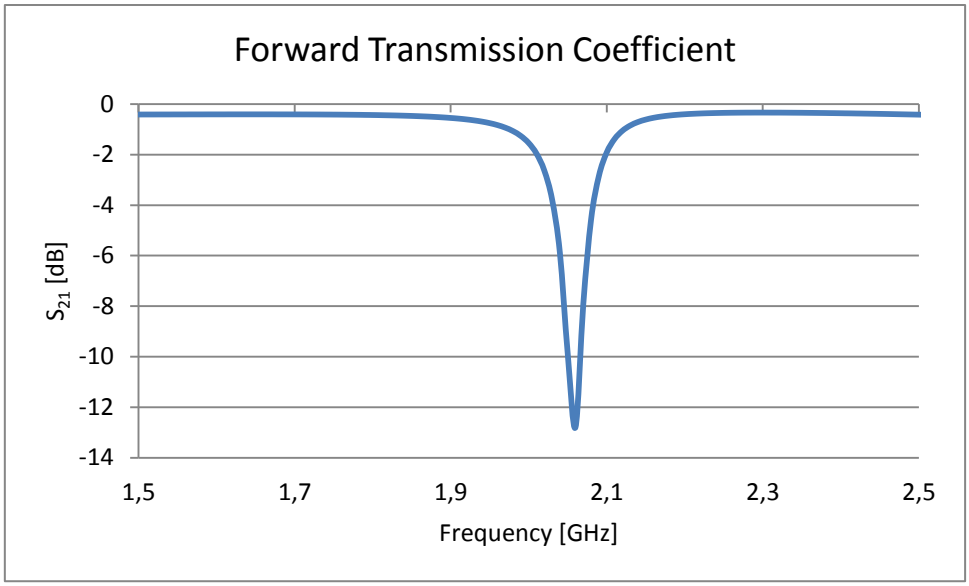

Figure 9: Forward transmission coefficient S_{21} of the simple split-ring resonator

Figure 9 shows the calculated forward transmission coefficient S_{21} in dB dependent on the frequency. The minimum of the scattering parameter is at the resonant frequency, which is 2.06GHz. At resonance, the wave is able to couple into the resonator structure and the electric field is concentrated in the gap of the split-ring resonator [7]. The transmitted wave at port 1 is higher than the received wave at port 2: $a_1 \gg b_2$. As a result, the scattering parameter $S_{21} = b_2/a_1$, which can be calculated using formula (50), decreases towards zero which leads to a negative value in the decibel scale.

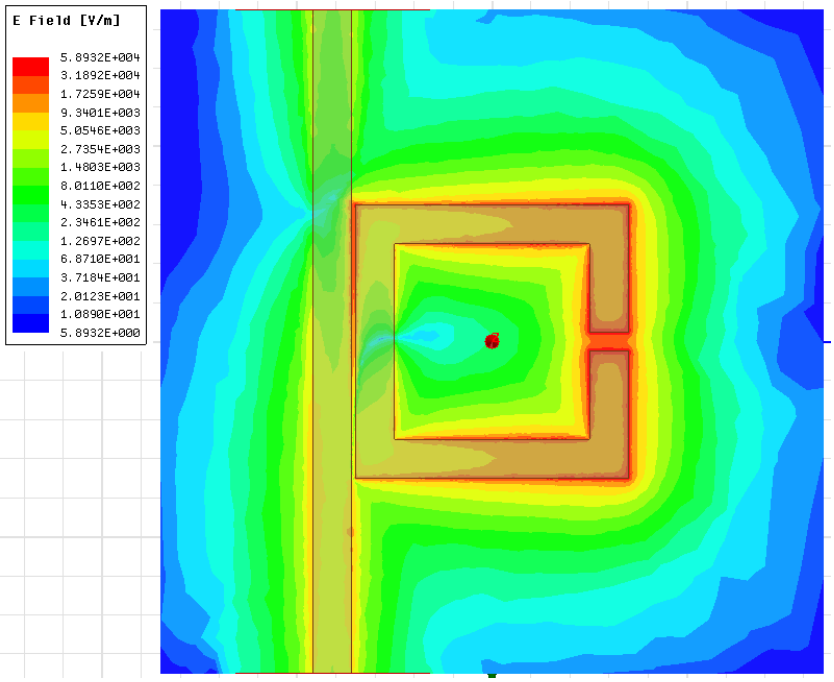

Figure 10: Electric field at resonance (f=2.06GHz). The electric field is highest at the gap of the split-ring resonator.

Figure 10 shows the electric field at resonance. The electric field is concentrated in the gap of the split-ring resonator. The magnitude of the electric field is only a numerical value and is depicted without consideration of any physical effect (Figure 10 and Figure 11).

If the frequency is not at resonance, almost all power is transmitted from transmitter to receiver, which means $a_1 \approx b_2$. The field amplitude in the gap of the split-ring is very small:

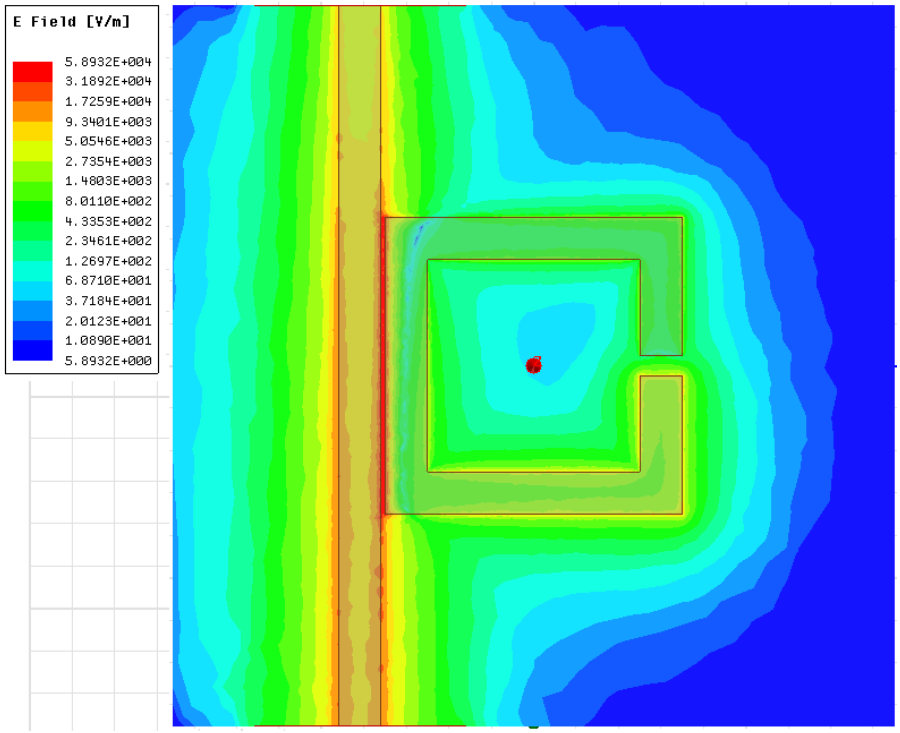

Figure 11: Electric field in V/m at a frequency that does not equal resonant frequency (f=1GHz). The electric field is concentrated along the microstrip line.

Figure 11 shows the electric field at a frequency of 1GHz, which does not equal the resonant frequency. The electric field is concentrated along the microstrip line. The field amplitude in the gap of the split-ring resonator is very low.

3.3.1. Model Validation

To validate the model built in HFSS, the forward transmission coefficient S_{21} of the simple geometry shown in Figure 1 was measured with a network analyzer (ZVB 4 Vector

Network Analyzer, Rohde & Schwarz GmbH & Co. KG) and compared to the calculated forward transmission coefficient shown in Figure 12.

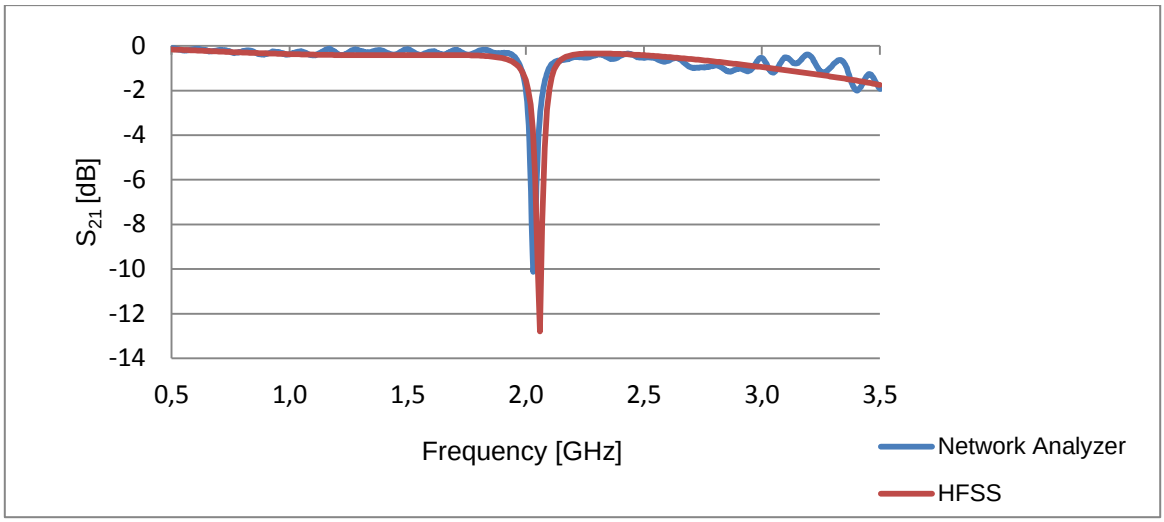

Figure 12: Measured (blue) and calculated (red) forward transmission coefficient S_{21} of the split-ring resonator.

There is only a slight shift in frequency between the measured and the simulated SRR forward transmission coefficients S_{21}. To make a mathematical statement, the correlation coefficient between the data and the P-value will be determined. The P-value is the probability that these data can be observed even if the transmission factors were unrelated. Therefore a low P-value corresponds to a high significance of the relation. The correlation coefficient between the data is 0.826 and the P-value is much less than 0.01. So the relationship between the data is highly significant. The measured resonant frequency accounts for 2.03GHz which yields a difference to the calculated resonant frequency of 1.5%. The mean error ϵ between simulated and measured data is given by

$$\epsilon = \frac{\sum_i \left| S_{21,sim}(f_i) - S_{21,meas}(f_i) \right|}{n} \tag{61}$$

with $S_{21,sim}(f_i)$ denoting the simulated S-parameter S_{21} at frequency f_i in dB and $S_{21,meas}(f_i)$ denoting the measured S-parameter S_{21} at frequency f_i in dB. The mean error between the measurement and the simulation accounts for 0.1 for 301 data points and equidistantly distributed frequencies from 0.5GHz to 3.5GHz.

3.3.2. IMPROVEMENT OF THE SIMPLE GEOMETRY

Parts of this chapter have already been presented in [29] and have been reproduced with permission of the coauthors. Content which was not generated by the author of this thesis is explicitly denoted.

At resonance the forward transmission coefficient S_{21} of the split-ring resonator shows a narrow dip where the high frequency energy is stored in the resonator and not transmitted via the microstrip line. The width of the resonance dip (3dB-bandwidth) is proportional to the Q-factor Q_f which is the ratio of center frequency to 3dB-bandwidth and should be optimized for sensor applications:

$$Q_f = \frac{f_0}{f_{3dB}} \tag{62}$$

The goal is to get a high Q-factor which implies a small bandwidth. A higher Q-factor leads to a better frequency resolution of the sensor device.

The aim of this section is to improve the Q-factor of the structure by varying different geometry parameters. The influence of the resonator gap size and the resonator line width on the Q-factor of the SRR is examined. The Q-factor is calculated using formula (62). The procedure of varying the geometric parameters and calculating the corresponding Q-factors is driven by a Python-Script. It consists of three main parts: the determination of the resonant frequency of the structure using the HFSS *Eigenmode* solver, the calculation of the forward transmission coefficient S_{21} at a frequency sweep around the solution frequency obtained with the *Eigenmode* solver using the HFSS *Driven Modal* solution type and the calculation of the quality factor by using formula (62).

Figure 13 shows the dependency of the Q-factor on the size of the resonator gap. The correlation coefficient is -0.936, and the P-value is much less than 0.01. The simulations are performed using a resonator width of 2mm. All other geometric dimensions are as described in section 3.3.

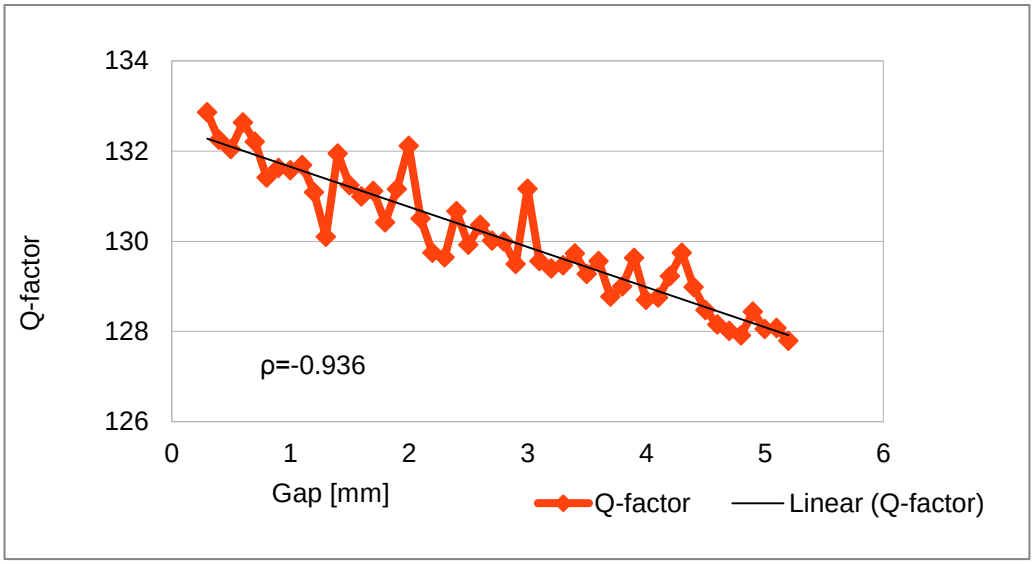

Figure 13: Q-factor dependent on the gap of the split-ring resonator (SRR).

Figure 14 shows the Q-factor dependent on the resonator width. The correlation coefficient of these parameters is even higher: -0.996, and again the P-value is much less than 0.01. This shows that the quality factor of the resonator strongly depends on both parameters. In these simulations, the resonator gap accounts for 1mm and the other dimension remain unchanged.

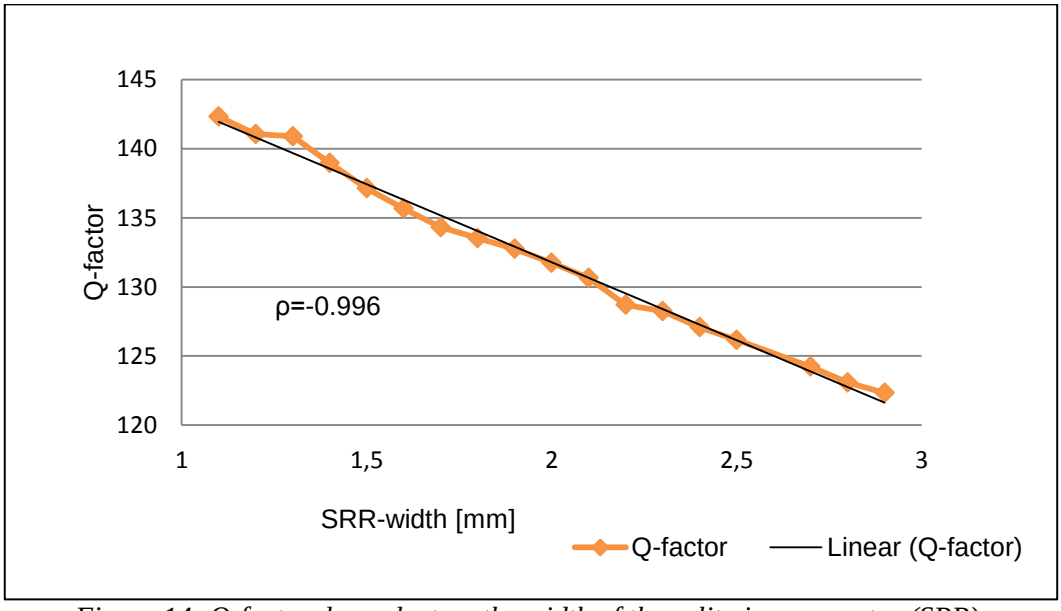

Figure 14: Q-factor dependent on the width of the split-ring resonator (SRR).

The result of this first parameter variation is that a higher gap and higher width lead to a decrease of the Q-factor. To get further insight on how a combined change of resonator gap and width influences the Q-factor, both parameters are varied simultaneously in a next

step. The result of these simulations is depicted in Figure 15. The highest Q-factor is reached at a gap of 1.1mm and a resonator width of 0.5mm. It accounts for 152.7.

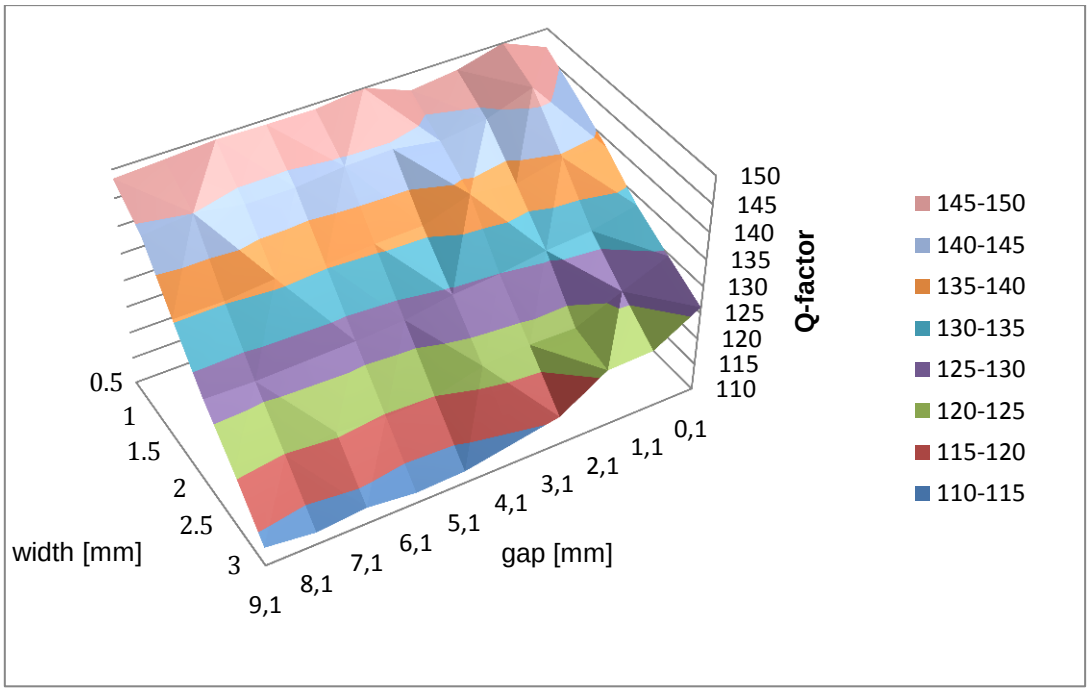

Figure 15: Result of the gap-width variation of the simple SRR.

Further, the resonant frequency of the geometry for the gap-width variation is calculated. The result is shown in Figure 16. With increasing gap size and resonator width, the capacitance and inductance decrease and therefore the resonant frequency increases.

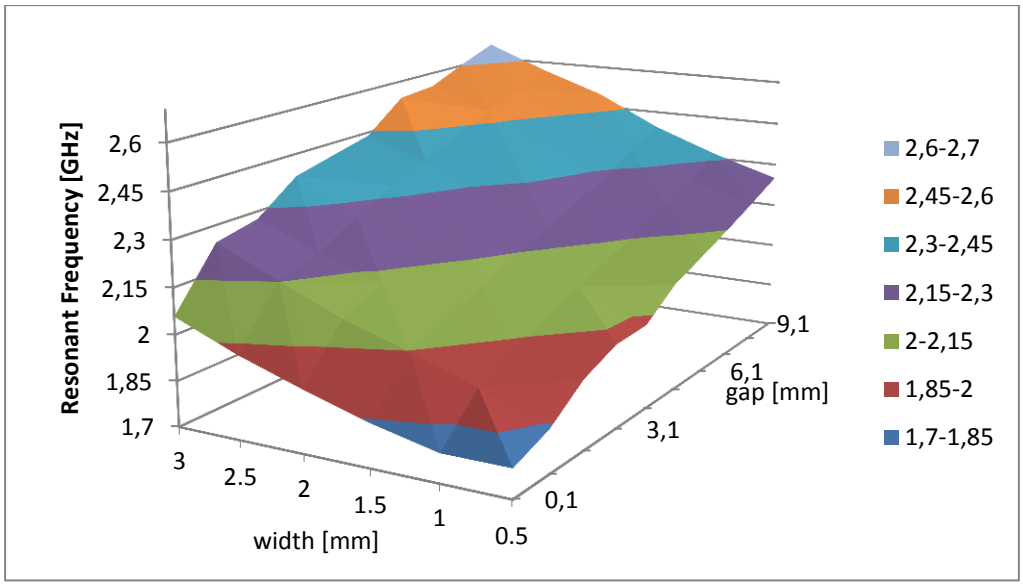

Figure 16: Resonant frequencies for the simple SRR with different gap size/resonator width.

3.4. INTRODUCTION TO MORE COMPLEX GEOMETRIES

In the next section, more complex geometries will be regarded to further increase the Q-factor. At this point, they will be introduced. Both structures will be further discussed in section 4.

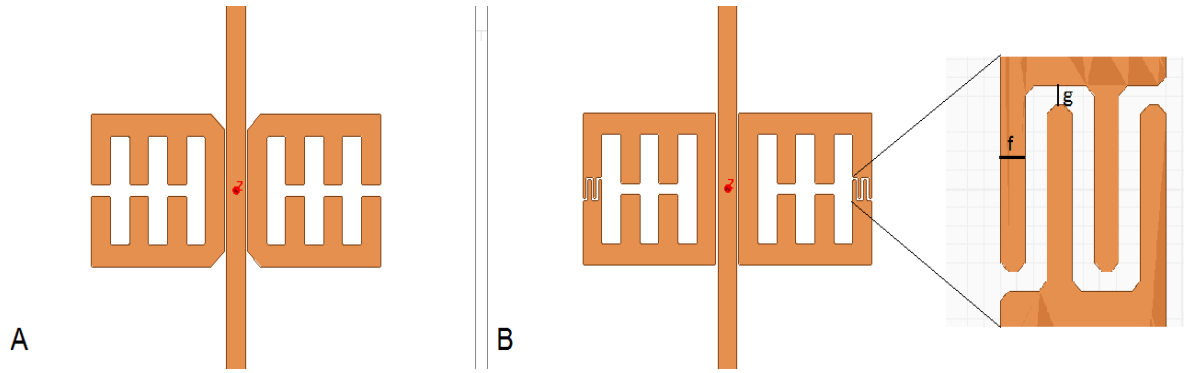

*Figure 17: **A)** Geometry of the centered-gap SRR. **B)** Interdigital centered-gap SRR. On the right side an enlarged view of the interdigital structure at the outer fingers is portrayed.*

CENTERED-GAP SPLIT-RING RESONATOR

The geometry of a centered-gap split-ring resonator is depicted in Figure 17A. The resonant frequency is expected to be lower than the resonant frequency of the basic structure because the capacitance of the centered-gap structure is higher. For this type of split-ring resonator a higher Q-factor and therefore a higher sensitivity of the biosensor than for the conventional type is expected [30].

INTERDIGITAL CENTERED-GAP SPLIT-RING RESONATOR

The interdigital centered-gap split-ring resonator is shown in Figure 17B. The interdigital structure at the outer fingers consists of 4 interdigital elements and is expected to further increase the capacitance and therefore sensitivity of the biosensor.

4. Optimization of the Split-Ring Resonator in HFSS

Parts of this chapter have already been presented in [31] and have been reproduced with permission of the coauthors. Content which was not generated by the author of this thesis is explicitly denoted.

In this section, the structures introduced in section 3.4 will be optimized in terms of their Q-factor. For both structures, the resonator line width and the gap size will be varied and the resulting quality factor will be calculated using the procedure described in section 3.3.2. In case of the interdigital centered-gap split-ring resonator, the width of the interdigital elements and the distance between them will be varied, too. After having found the geometry with the highest Q-factor for each design, one structure is chosen to be manufactured and the model will be validated.

4.1. Centered-Gap Split-Ring Resonator

As expected, the Q-factor of the centered-gap split-ring resonator is higher than the Q-factor of the conventional SRR. So we optimized this structure in terms of its Q-factor. Figure 18 shows a plot of the Q-factor of the centred-gap SRR in dependency on the gap and the resonator width. It reaches its peak when the gap is 5mm and the width is 2mm and it accounts for 254.1.

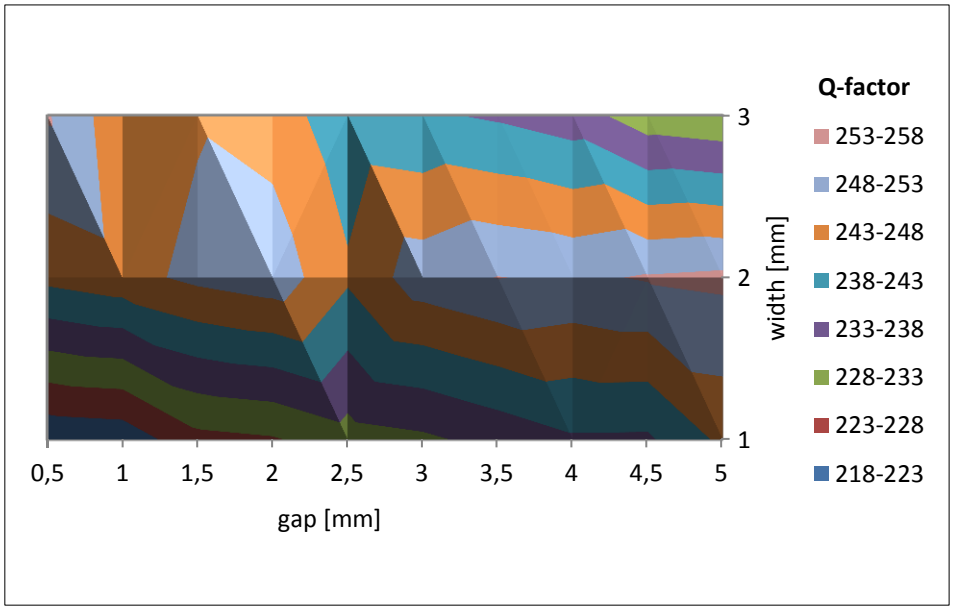

Figure 18: Q-factor dependent on the resonator width [mm] and the gap [mm] of the centered-gap split-ring resonator.

The resonant frequency of the structure with the highest quality factor is 2.0718GHz. The plot was generated using the calculated values obtained with the python script described in section 3.3.2. Since HFSS did not converge for two gap-width combinations, the Q-factor was calculated using univariate regression in the statistics software DataLab. This procedure was necessary for a gap of 4mm in combination with a resonator width of 1mm and a gap of 4.5mm in combination with a resonator width of 2mm.

4.2. INTERDIGITAL CENTERED-GAP SPLIT-RING RESONATOR

In this section, the improvement of the quality factor of the interdigital centered-gap split-ring resonator is described. Primarily, the Q-factor is improved by varying the gap and width of the resonator. The default values of the width of the interdigital elements, which is denoted f in Figure 17B, and the distance between the interdigital elements, denoted g in Figure 17B, are set to $f = 0.3$mm and $g = 0.2$mm. The length of the interdigital elements equals resonator width.

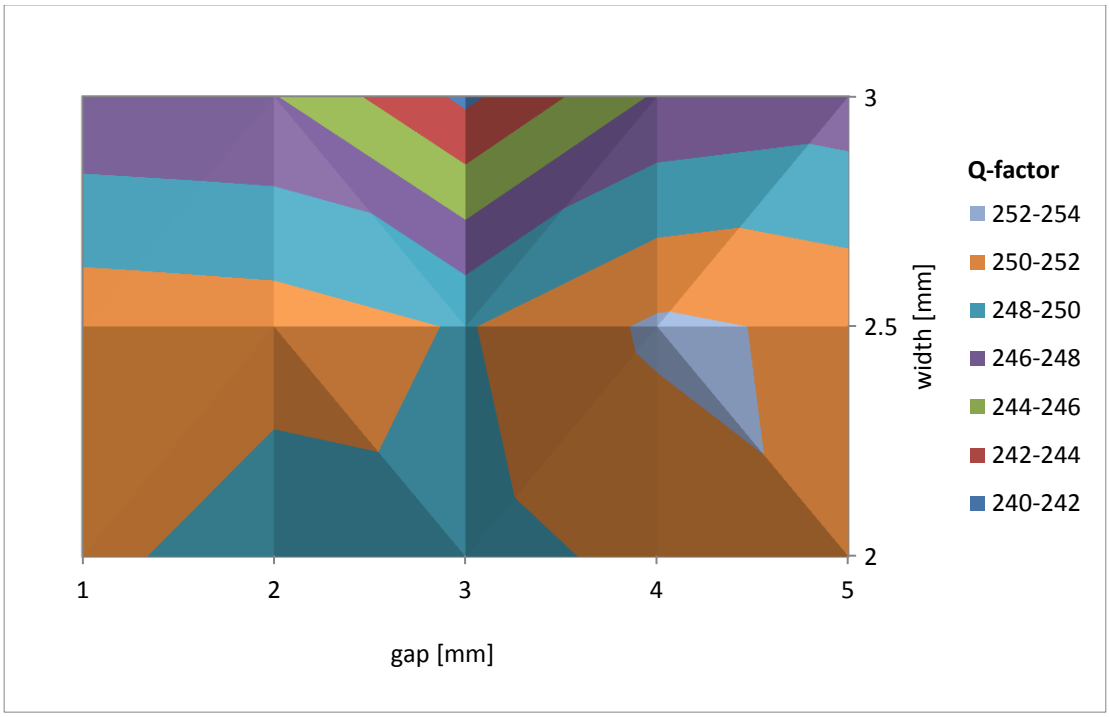

Figure 19: Q-factor dependent on the resonator width [mm] and the gap [mm] of the interdigital centered-gap split-ring resonator.

The highest Q-factor was reached at a gap of 4mm and a resonator width of 2.5mm. It accounts for 252.4 which is slightly lower than the quality factor of the centered-gap split-ring resonator. The resonant frequency of the structure is 1.78331GHz.

To further increase the capacitance and consequently the Q-factor, the width of the interdigital elements and the gaps between them were varied with the gap and width of the resonator set to 4mm and 2.5mm. Now a slightly increased Q-factor of 257.1226 at an interdigital width of 0.45mm and an interdigital gap of 0.2mm can be observed. The resonant frequency of the improved structure is 1.7545GHz.

After having found the structure with the highest Q-factor, the structure is modified a bit to save material and cost. It has to be figured out if the same structure as shown in Figure 17B with only one split-ring offers a high Q-factor as well.

Following results can be obtained from the simulation with the same geometric parameters as were found to be the best for the interdigital centered-gap split-ring resonator: a Q-factor of 244.564 which is slightly lower and a resonant frequency of 1.7817GHz.

4.3. EXPERIMENTAL VALIDATION

For the experimental validation, the structure with the highest quality factor is manufactured. The chosen geometries are the one-sided and the two-sided interdigital centered-gap resonator with a gap size of 4mm, a resonator width of 2.5mm, an interdigital gap of 0.2mm and an interdigital width of 0.45mm.

The forward transmission coefficient of the structure was measured using a network analyzer. The comparison of the measured and the calculated forward transmission coefficients is shown in following plot:

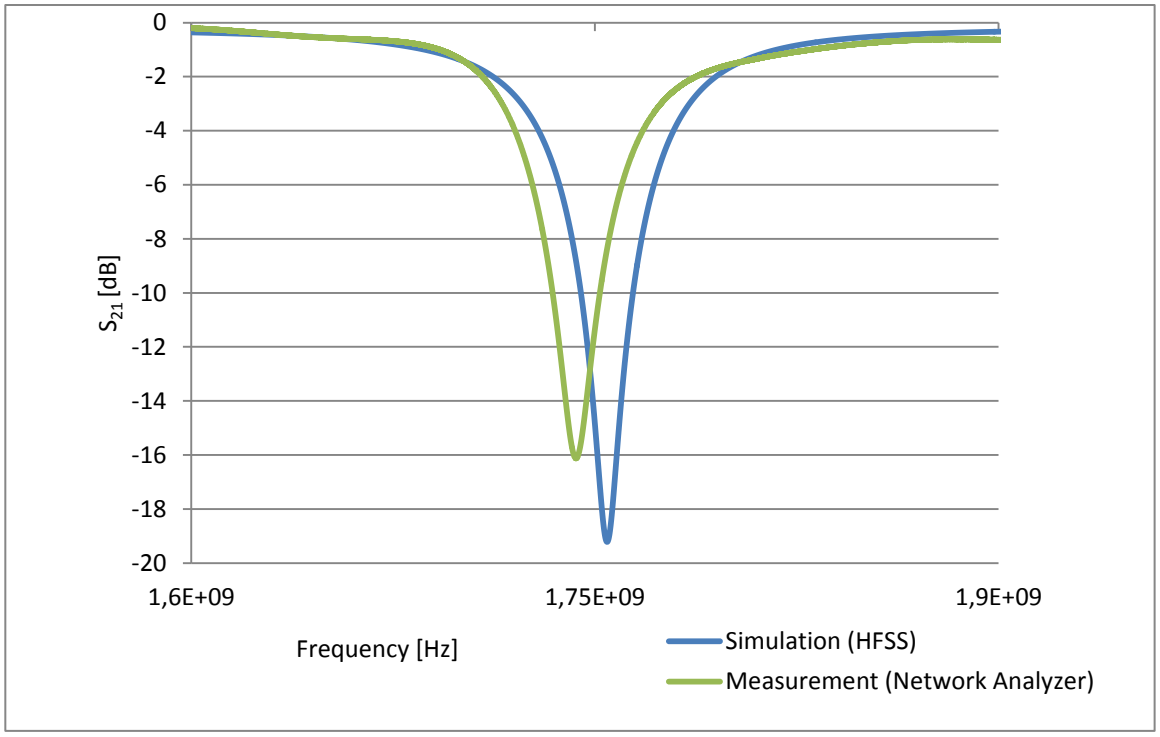

Figure 20: Comparison of the measured (green) and simulated (blue) S-parameter S_{21} of the interdigital centered-gap split-ring resonator.

These curves feature a correlation coefficient of 0.816 and a P-value of 0. The measured resonant frequency is 1.74305GHz whereas the resonant frequency calculated by HFSS is 1.7545GHz which yields a difference of 0.7%. The Q-factor of the manufactured structure is calculated using Matlab (MathWorks, Inc., USA) via the 3dB bandwidth and results to 179.9497. The mean error between measurement and simulation is calculated using formula (61) and accounts for about 1.1 for 3001 data points and equidistantly distributed frequencies from 1.6GHz to 1.9GHz.

Additionally, the same structure placed on only one side of the microstrip line is manufactured and its forward transmission coefficient S_{21} is measured to validate the simulation model:

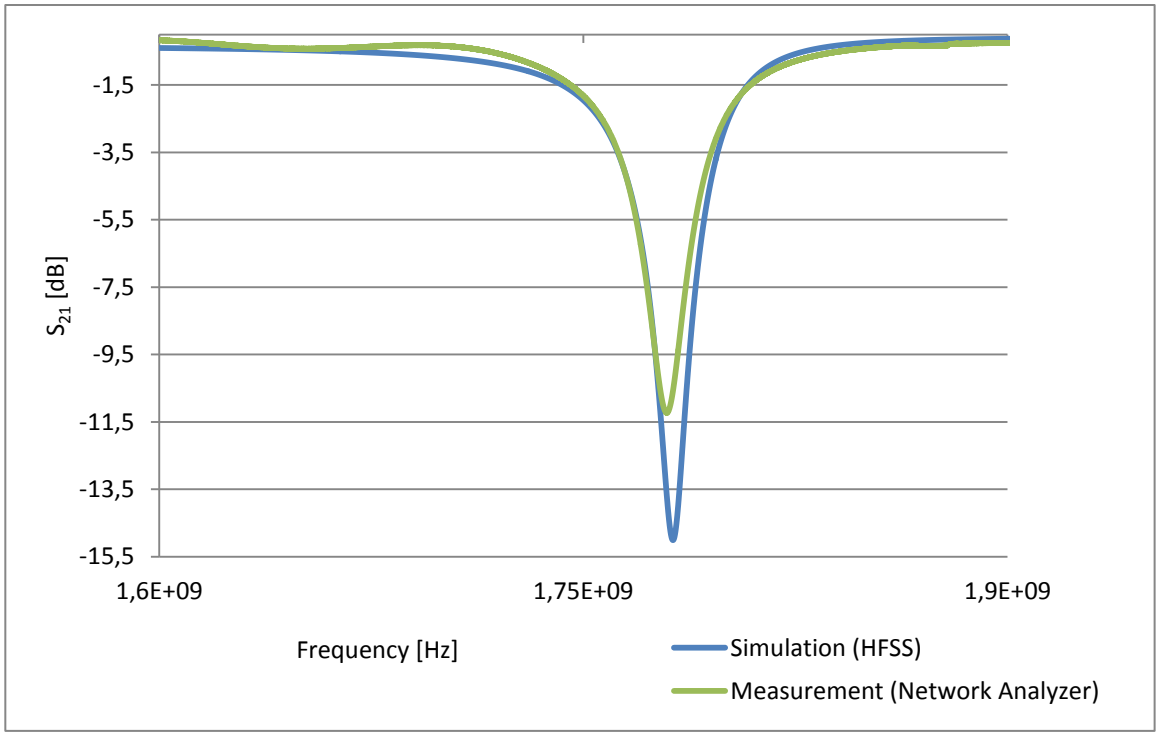

Figure 21: Comparison of the measured (green) and simulated (blue) S-parameter S_{21} of the interdigital centered-gap split-ring resonator placed only on one side of the microstrip line.

These curves feature a correlation coefficient of 0.46 and a P-value of 0. The measured resonant frequency is 1.77946GHz whereas the resonant frequency calculated by HFSS is 1.7817GHz which yields a percentage error of 0.13%. The Q-factor of the manufactured structure is calculated using Matlab and the result is 155.3027. The mean error between measurement and simulation accounts for 0.32.

4.4. Further Adaption of the Simulation Model

In section 4.3, the resonant frequencies and Q-factors of the measured and manufactured structures are compared. The differences between the resonant frequencies are very small (below 1%), whereas the differences between the Q-factors are high: 42.89% for the two-sided resonator and 57.48% for the one-sided resonator. To reduce the error in further simulations, the HFSS model will be adapted to the measurement. A possible reason for the differences between model and manufactured structure is that the electromagnetic parameters of the substrate used in the simulations don't match the real electromagnetic parameters. The parameters in the model are adopted from the RO4350B™ datasheet which can be found online. They are given for distinct frequencies which are higher than

the solution frequency used for the simulations. In this section the loss tangent of the Rogers substrate is varied to find a value which leads to smallest possible differences between Q-factor and resonant frequency. Only the model of the one-sided interdigital centered-gap split-ring resonator will be adapted to the measurement because this structure is chosen to be further investigated.

The model is simulated with loss tangents of 0.0031 (adopted from the Rogers datasheet), 0.005, 0.0055 and 0.006. Following graph shows the percentage errors between the results of the simulations and the measurement of the manufactured structure:

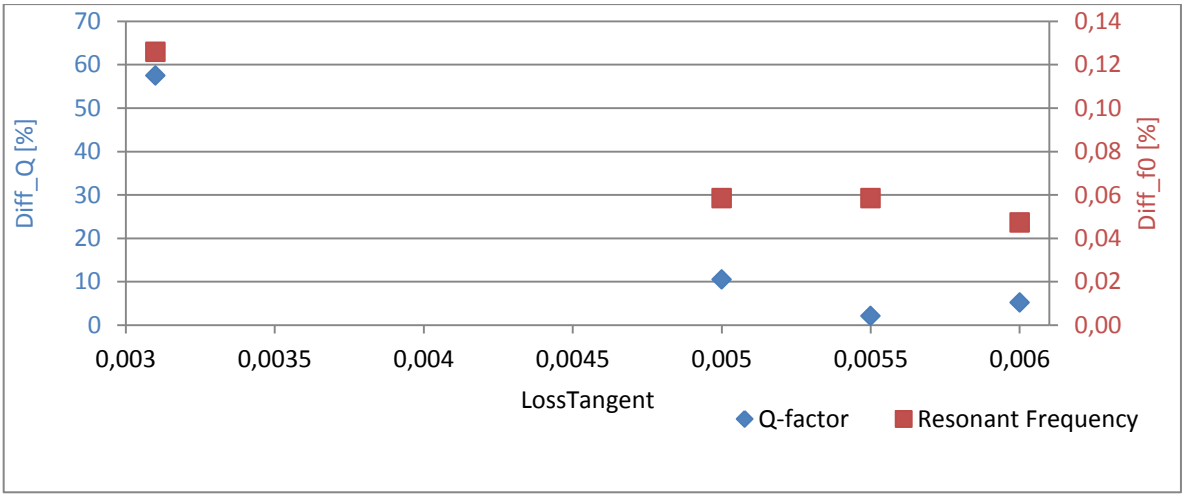

Figure 22: Percentage errors between the simulations and measurement with varying loss tangent: blue data points show the percentage error of the Q-factor (labelled by the primary vertical axis on the left) and the red data points denote the percentage error of the resonant frequency (labelled by the secondary vertical axis on the right).

The percentage errors of the resonant frequency are beyond 0.13% for all values of loss tangent. A clear improvement is reached regarding the Q-factor: the high error of 57.48% with the loss tangent adopted from the datasheet can be reduced to values below 10% for loss tangents of 0.0055 and 0.006. An overview of the absolute and percentage errors between measurement and simulations is given in Table 1. The smallest error regarding resonant frequency is reached with a loss tangent of 0.006. It accounts for 0.84MHz which corresponds to 0.0472%. For the Q-factor, the smallest error is reached with a loss tangent of 0.0055 with a difference of only 3.1828 corresponding to 2.0494%. Calculating the mean between the percentage error of the resonant frequency and the Q-factor, one gets 1.0539% for a loss tangent of 0.0055 and 2.5992% for a loss tangent of 0.006. Therefore the loss tangent of 0.0055 is chosen for further simulations. The mean error between simulation and measurement could be decreased to 0.27 calculated for 3001 equidistantly

distributed data points from 1.6GHz to 1.9GHz. The correlation coefficient accounts for 0.996 with a P-value of 0.

Table 1: Comparison of measurements and simulations with varying loss tangent.

		Absolute value	Error	Error [%]
Resonant Frequency	Measurement	1.7796GHz	-	-
	Simulation: $\tan \delta_L = 0.0031$	1.7817GHz	2.24MHz	0.1259%
	Simulation: $\tan \delta_L = 0.005$	1.7805GHz	1.04MHz	0.0584%
	Simulation: $\tan \delta_L = 0.0055$	1.7805GHz	1.04MHz	0.0584%
	Simulation: $\tan \delta_L = 0.006$	1.7803GHz	0.84MHz	0.0472%
Q-factor	Measurement	155.3027	-	-
	Simulation: $\tan \delta_L = 0.0031$	244.564	89.2613	57.4757%
	Simulation: $\tan \delta_L = 0.005$	171.6	16.2973	10.4939%
	Simulation: $\tan \delta_L = 0.0055$	158.4855	3.1828	2.0494%
	Simulation: $\tan \delta_L = 0.006$	147.3027	-8	-5.1512%

The next graph shows the measured and the simulated forward transmission coefficient S_{21} with loss tangent set to 0.0055 in the simulation:

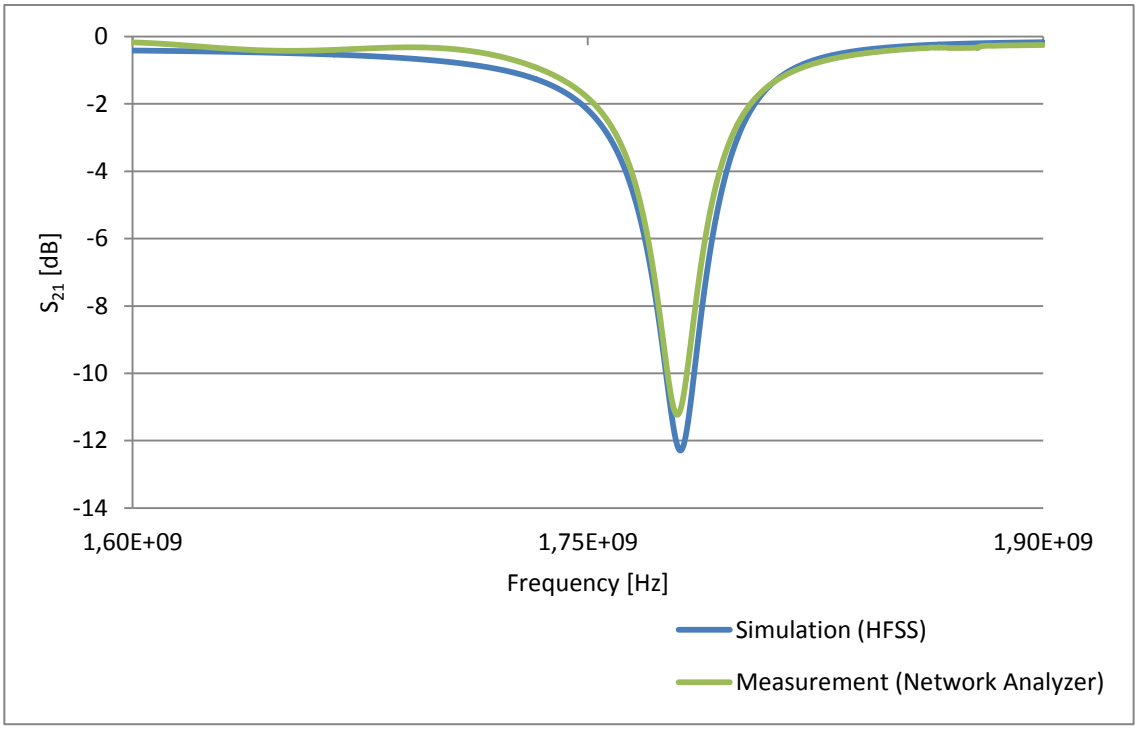

Figure 23: Comparison of the measured (green) and simulated (blue) S-parameter S_{21} of the interdigital centered-gap split-ring resonator placed only on one side of the microstrip line. The loss tangent in the simulation is set to 0.0055.

4.5. EQUIVALENT CIRCUIT

In this section, an equivalent circuit for the one-sided interdigital centered-gap split-ring resonator is built and adapted to the manufactured resonator. The used software is Microwave Office from AWR Corporation which is an electronic design automation software company. The microstrip line is modelled using a PI-structure consisting of a resistance and an inductance and is coupled to the resonator structure via two capacitors. The resonator consists of coils and capacitors. The interdigital structure is modelled as capacitance parallel to a resistance. Microwave Office offers an optimization environment where equation and goals can be defined and optimized.

To adjust the equivalent circuit to the structure, the complex S-parameter S_{11} was measured while the structure was terminated with 50Ω in the frequency range from 1.7GHz to 1.82GHz with steps of 1MHz. The result of the measurement was imported to Microwave Office. The optimizer goal was the minimization of the variables D_{im} and D_{re} with the index im or re denoting the imaginary or real part of the S-parameter, and the index C or M denoting the calculated (via Microwave office) or measured S-parameter:

$$D_{im} := |S_{11,im,C} - S_{11,im,M}| \quad (63)$$

$$D_{re} := |S_{11,re,C} - S_{11,re,M}| \quad (64)$$

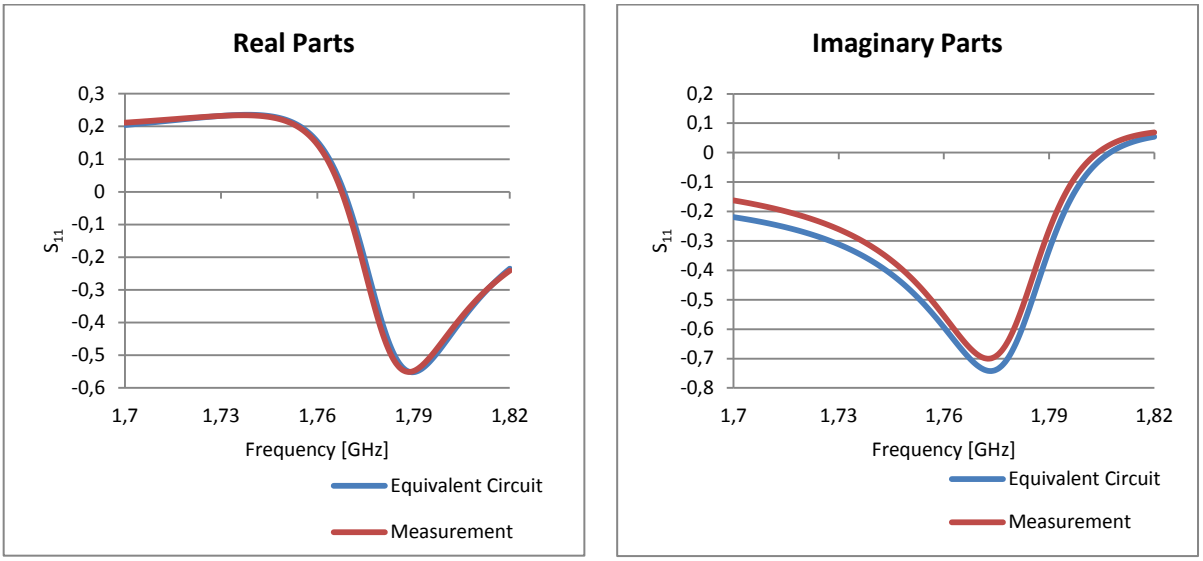

Figure 24: Real and imaginary parts of the manufactured one-sided centered-gap split-ring resonator and its equivalent circuit.

Figure 24 shows the real and imaginary parts of the scattering parameter S_{11} of the manufactured structure (red line) and its equivalent circuit (blue line).

The next plot shows the Smith diagram of the equivalent circuit and of the manufactured structure for comparison.

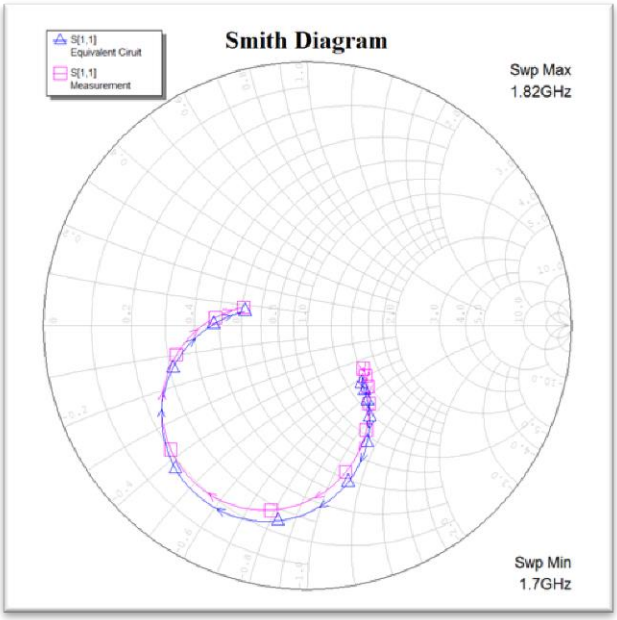

Figure 25: Smith diagram, generated in Microwave Office. The blue line shows the result of the equivalent circuit and the pink line shows the measurement result.

The mean error between manufactured structure and its equivalent circuit is calculated using formula (61). Following table shows the mean error of the real parts, the complex parts and the total mean error calculated for 121 equidistant frequency points in the range from 1.7GHz to 1.82GHz:

Table 2: Mean error between one-sided interdigital centered-gap SRR and its equivalent circuit.

Mean error (real parts)	Mean error (complex parts)	Mean error (total)
0.008588353	0.04660713	0.02759774

The optimization results in the equivalent circuit shown in Figure 26. The optimized values for the lumped elements are shown in following table:

Table 3: Lumped elements of the optimized equivalent circuit.

Resistance [Ω]		**Inductance [nH]**			**Capacitance [pF]**			
R	R1	L1	L2=L3	L4	C	C1=C3	C2	C4
4091	47.65	1.788	0.11	2.92	0.3975	0.9	3.624	3.013

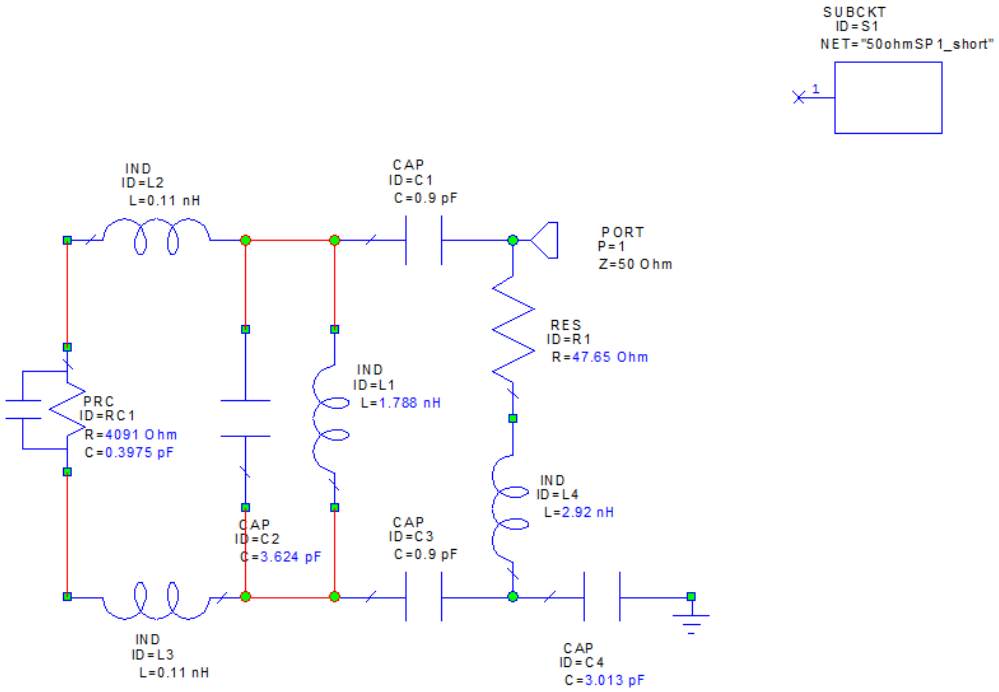

Figure 26: Equivalent circuit of the one-sided centered-gap split-ring resonator.

5. ADDITION OF THE BUFFER SOLUTIONS

Parts of this chapter have already been presented in [32] and have been reproduced with permission of the coauthors. Content which was not generated by the author of this thesis is explicitly denoted.

Having found the final geometry, the further setup of the sensor has to be looked at. The final application of the sensor will be the measurement of different marker proteins like CRP in blood plasma. For the first tests of the sensor, different buffer solutions which are similar to blood plasma or to the hydrogel matrix, which is used for the bio-functionalization (compare Figure 7) of the sensor in their composition will be used. These solutions have to be characterized in terms of their electromagnetic properties to get significant results.

5.1. ELECTROMAGNETIC CHARACTERIZATION

5.1.1. METHOD AND VALIDATION

Electric conductivity will be calculated using equation (13) and the loss tangent will be calculated using equation (20). In these formulas, complex permittivity is used which has to be measured. For the measurement the so-called 'Principle of Reflection Method' [10] is used. The reflection coefficient is measured on the interface between two materials: an open end of the coaxial line as detector and the material under test (MUT). The reflection coefficient depends on the dielectric parameters of the MUT. Figure 27 based on figure 1 from [10] shows the simplified measurement setup.

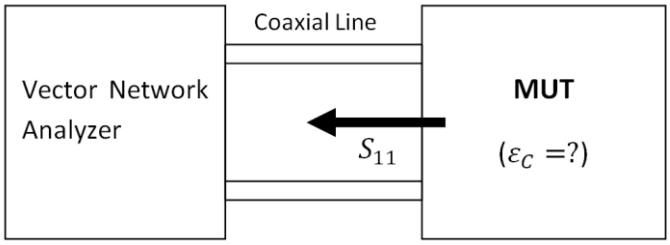

Figure 27: Measurement setup using the 'Principle of Reflection Method'. The detector (open-ended coaxial line) is placed on the surface of the MUT. The reflection coefficient contains information about the MUT which is needed to calculate complex permittivity. The illustration is based on figure 1 from [10].

Following relationships between the reflection coefficient S_{11}, the admittance Y and the permittivity ε are used [10]:

$$Y = j\omega\varepsilon C_0 + \sqrt{\varepsilon^5} G_0 \tag{65}$$

$$Y = \frac{Y_0(1 - S_{11})}{1 + S_{11}} \tag{66}$$

$$Y_0 = \frac{1}{50\Omega} \tag{67}$$

Y_0 is the characteristic admittance of the probe and C_0 and G_0 are constants defined by the measurement setup. These constants can be determined by measuring the S-parameters of a fluid with known permittivity at two frequencies, inserting the values for the S-parameters, permittivity and frequencies in formula (65) and (66) and solving for C_0 and G_0. The used solution is 98% Ethanol from which the complex permittivity at different frequencies is known [33]. Since two unknowns have to be calculated, two frequencies are to be used. A Matlab script is written to find the best frequencies for the calculation of C_0 and G_0 in terms of a result which fits the values from the literature best using the Euclidian norm in our frequency-range of interest (1GHz-2.5GHz). The measurements are performed at 25°C. Different amounts of 98% Ethanol (25ml, 35ml and 50ml) are used for the measurement. 50ml is set as maximum volume, because bigger amounts of the buffer solutions which will be measured later on have not been available. The solution is measured in a beaker with a diameter of approximately 6.5cm. The S-Parameters of 98% Ethanol are measured with the network analyzer at a temperature of 25°C at the same frequencies which are given in the literature. Following table shows the best matching parameters, the corresponding frequencies and the calculated Euclidian norm in the frequency-range of interest $||.||_{[1;2.5]}$. The columns correspond to the different amounts of Ethanol.

The setup with 50ml of Ethanol leads to the smallest error, so this amount will be used for further calculations.

Table 4: Best matching parameters for different amounts of 98% Ethanol.

[ml]	**25ml**	**35ml**	**50ml**
C0 · 10^{14}	-0.28-2.84i	-0.26-2.834i	-0.26-2.84i
G0· 10^{6}	-0.81-0.59i	-0.77-0.57i	-0.76-0.57i
Frequency 1 [Hz]	1.20E+09	1.20E+09	1.20E+09
Frequency 2 [Hz]	1.80E+09	1.80E+09	1.80E+09
$\|\|\cdot\|\|_{[1;2.5]}$	8.14E-03	7.40E-03	7.14E-03

After determining C_0 and G_0 the results of the permittivity calculation of ethanol are compared at all frequencies with the given values found in literature [33]. The result of the comparison is shown in Figure 28 where the permittivity is plotted between 1GHz and 2.5GHz.

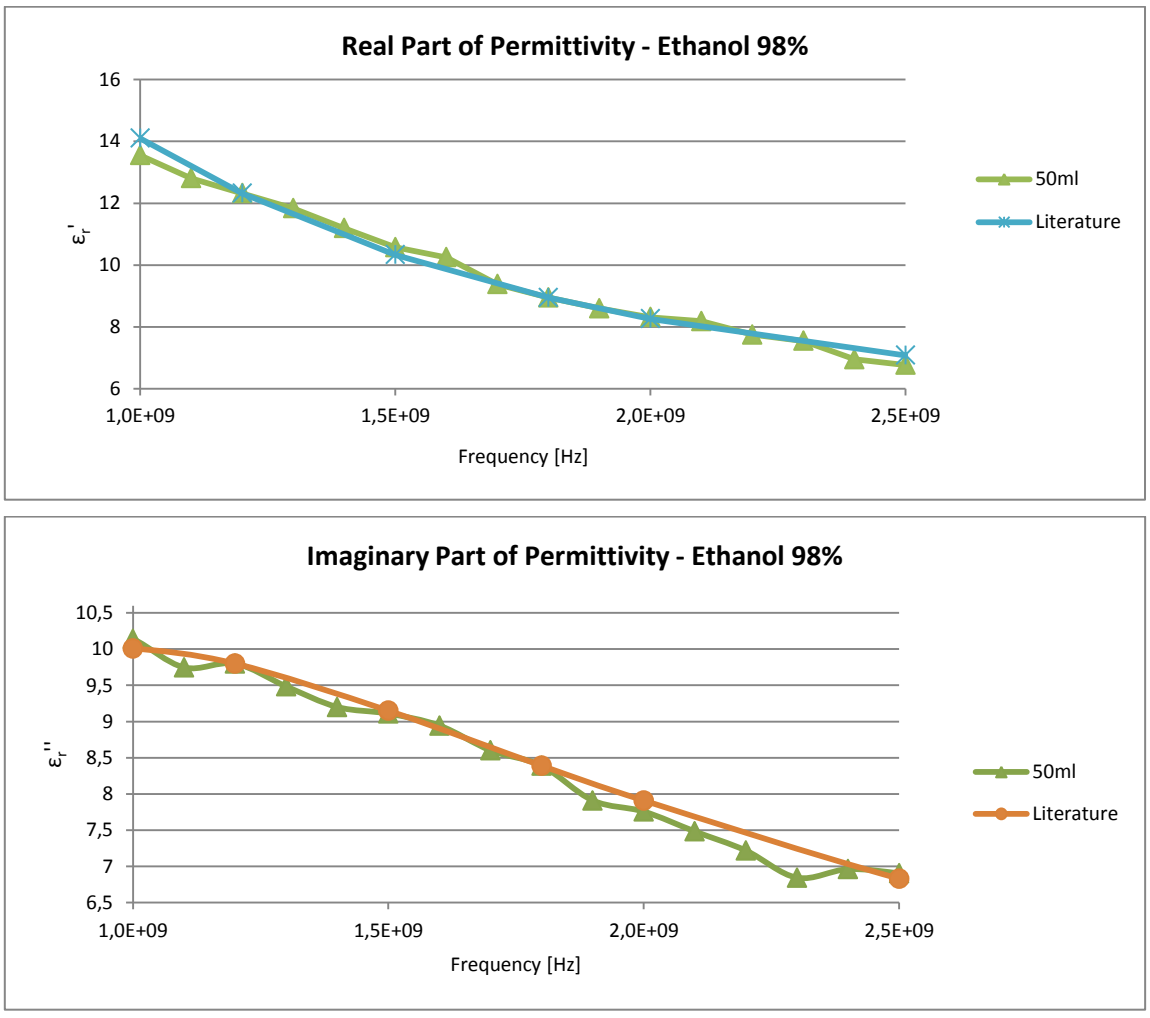

Figure 28: Comparison of ethanol permittivity. ε_r' ... real part of complex permittivity, ε_r''... imaginary part of complex permittivity.

To decide whether there is a significant difference between measured data and the values from literature a t-test will be performed. It is carried out by the statistics software SigmaStat (Systat Software Inc.). First the real parts of the calculated permittivity in the frequency range of interest (1GHz to 2.5GHz) are compared to the values found in literature. Then the same test will be performed for the complex parts. The results of the t-tests for the reals and imaginary parts are that there are no significant differences between the measured and the calculated values, using a level of significance of 0.05.

The conclusion of the results of the t-tests is that there is no significant difference between the calculated values and the values extracted from literature, which means that the calculations match the real values with high accuracy. So the procedure for permittivity measurement could be validated.

5.1.2. Characterization of the Buffer Solutions

The above described procedure is used to calculate the complex permittivity of nine different buffer solutions. Their properties are listed in the table below:

Table 5: Buffer solutions and their properties

Name	Compounds	pH
10mM TRIS[1]	10mM TRIS, 50mM NaCl, 2mM CaCl2	7.3
50mM TRIS	50mM TRIS, 150mM NaCl	7.3
25mM Carbonate	25mM carbonate, 100mM NaCl, 3.2mM CaCl2	7.3
9.6mM PBS	9.6mM phosphate, 137mM NaCl, 2.7mM KCl	7.3
D1TRIS10	20% (w/w) dextran in 10mM TRIS	7.3
D2TRIS10	10% (w/w) dextran in 10mM TRIS	7.3
D3TRIS10	5% (w/w) dextran in 10mM TRIS	7.3
D4TRIS10	2.5% (w/w) dextran in 10mM TRIS	7.3
D5TRIS10	1.25% (w/w) dextran in 10mM TRIS	7.3

[1] Tris(hydroxymethyl)-aminomethan

The used equation (66) leads to five complex solutions. The real and imaginary part of complex permittivity can't be negative, so a few solutions can be immediately excluded. This is done in Matlab using following commands:

```
eps=eps(real(eps)>=0);
eps=eps(imag(eps)>=0);
```

Now either one or two of the five solutions are left. In the first case, the right solution is found. In the second case, both solutions have to be looked at and the physically more reasonable values have to be determined. Following pictures show the results of the permittivity calculation and the electromagnetic characterization of two of the buffer solutions as an example.

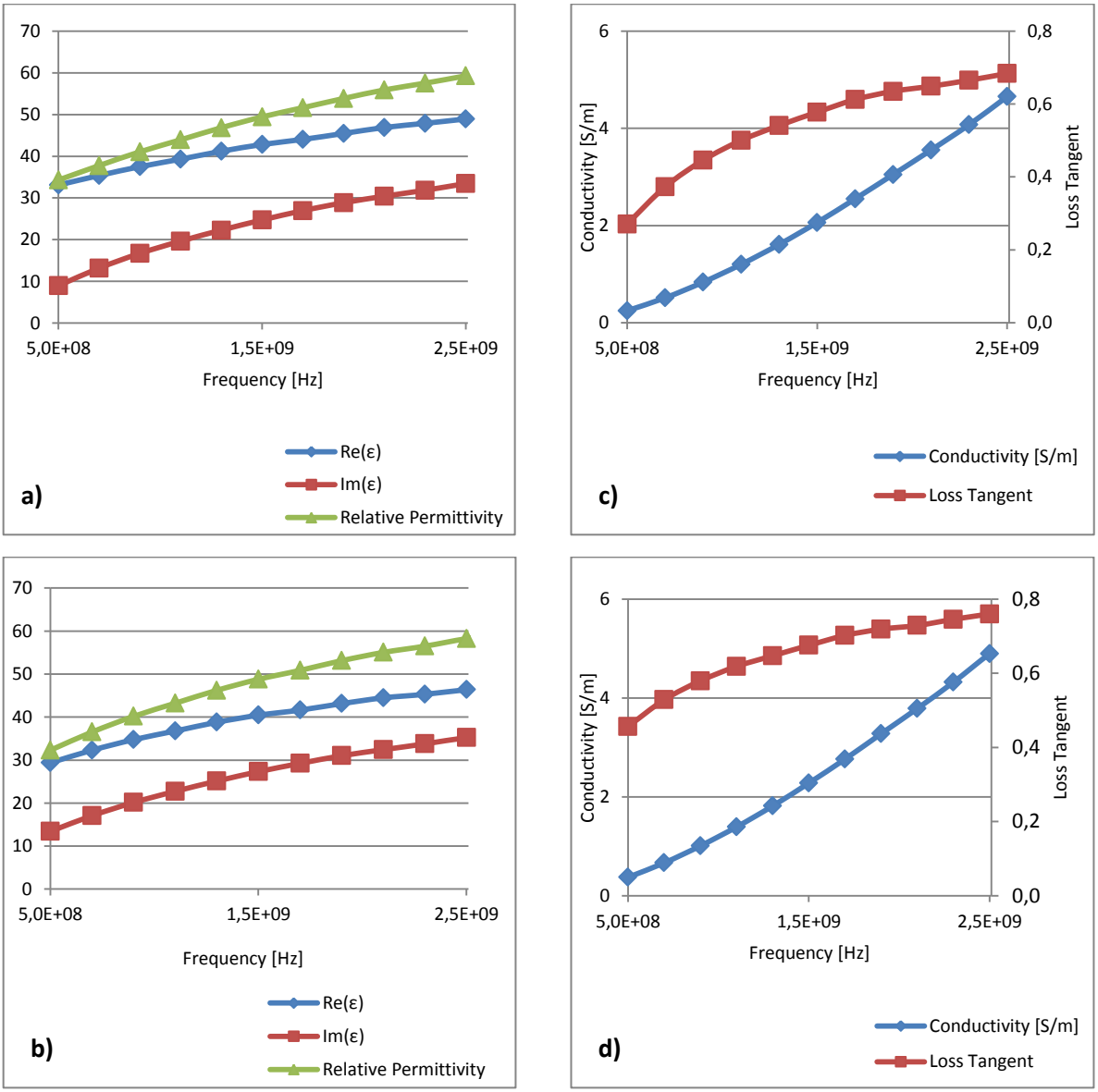

Figure 29: a)-b): Real part and imaginary part of complex permittivity and relative permittivity, c)-d): conductivity [S/m] and loss tangent of two buffer solutions. a) and c) show the properties of the carbonate buffer, b) and d) show the D3TRIS10 buffer.

Figure 29a) and c) show the electromagnetic characterization of the carbonate buffer and Figure 29b) and d) show the characterization of the D3TRIS10 buffer. The D3TRIS10 buffer is similar to the hydrogel matrix which is used for the bio-functionalization (compare section 2.3) of the sensor. The surface modification process is further described in [24]. The carbonate buffer is similar to blood plasma in its composition, but without human serum albumin. Following table shows the main components of blood plasma [34, 35, 36]:

Table 6: Components of blood plasma.

Components	Plasma
pH	7.4
H_2O %	90-93
Na^+	135-155 mmol/l
Cl^-	100-120mmol/l
Ca^{2+}	1.2-5.2 mmol/l
$PO4^{3-}$	1.2-2.2 mmol/l
K^+	3.5-5.5 mmol/l
HCO^{3-}	25 mmol/l
Total Protein	60-80 mg/ml
Human Serum Albumin (HSA)	40-50 mg/ml

The electromagnetic permittivity of the D3TRIS10 buffer and the carbonate buffer are rather similar to each other. The real and imaginary part of complex permittivity increase with increasing frequency which results in an increasing relative permittivity. The real part of complex permittivity of the carbonate buffer is slightly higher than the real part of complex permittivity of the D3TRIS10 buffer. The imaginary part of complex permittivity is slightly higher for the D3TRIS10 buffer.

Both the D3TRIS10 buffer and the carbonate buffer will be used for the analysis of the sensor response to the buffer solution.

5.2. POSITIONING OF THE BUFFER DROPLET

In this chapter the sensing area of the resonator will be determined. The resonant frequency of the SRR depends on the inductance and the capacitance, compare formula (53). The permittivity of the sample, which is one of the above described buffer solutions, directly influences capacitance, as described in [20]. The small gaps lead to a high electric field amplitude. For illustration, the electric field of the one-sided interdigital centered-gap resonator at the simulated resonant frequency, $f_0 = 1.7805\text{GHz}$, is simulated using HFSS. The magnitude of the electric field is only a numerical value and is depicted without consideration of any physical effect (Figure 30, Figure 31 and Figure 32).

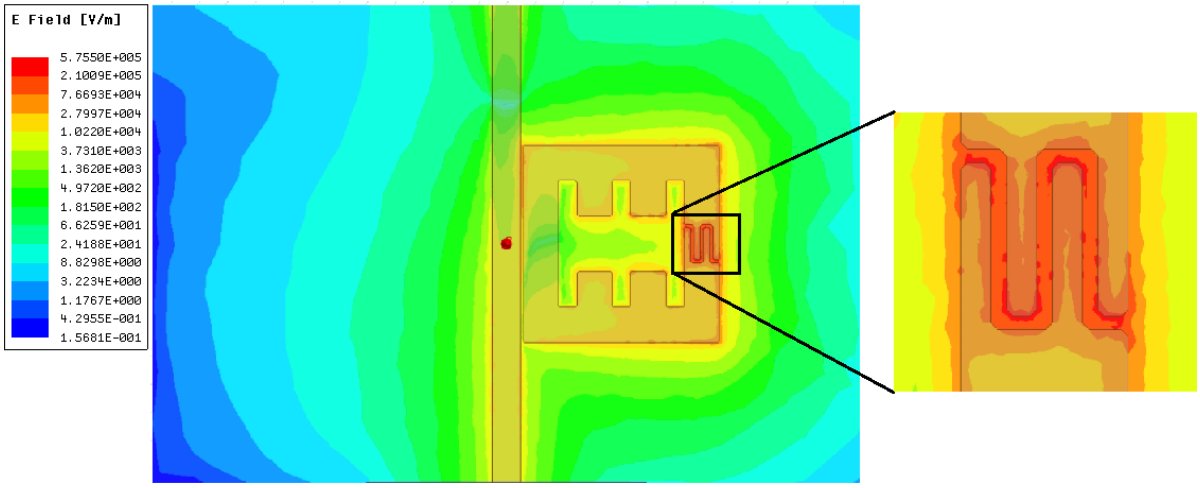

Figure 30: Electric field of the one-sided interdigital centered-gap split-ring resonator in V/m at resonance (f= 1.7805GHz).

The highest electric field amplitude occurs in the area of the interdigital structure marked by a black rectangle in Figure 30. Figure 31 shows the electric field printed on a vertical plane, outlined at the upper right part in Figure 31.

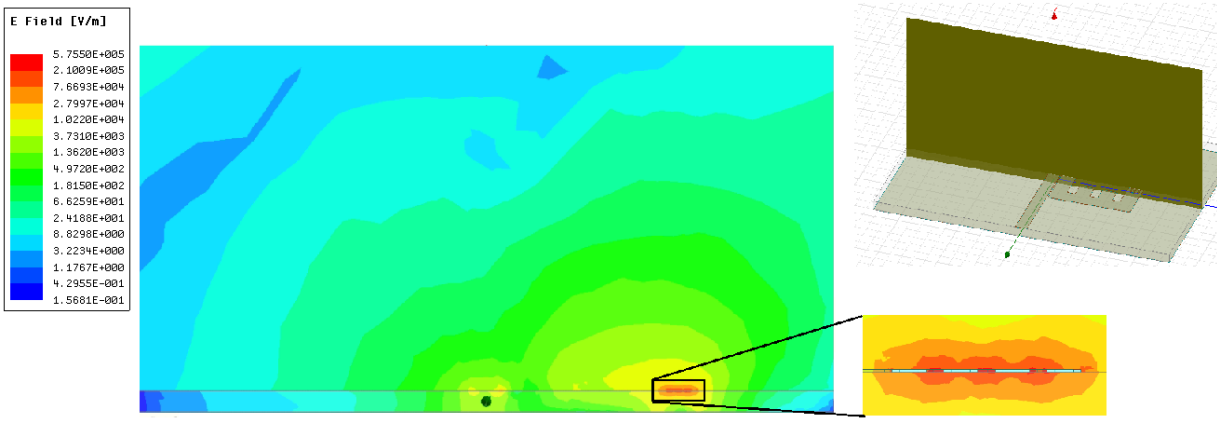

Figure 31: Electric field printed on the vertical plane in V/m at resonance (f=1.7805GHz).

For comparison, the electric field of the one-sided centered-gap split-ring resonator is shown at 1GHz as an example for the field at non-resonance:

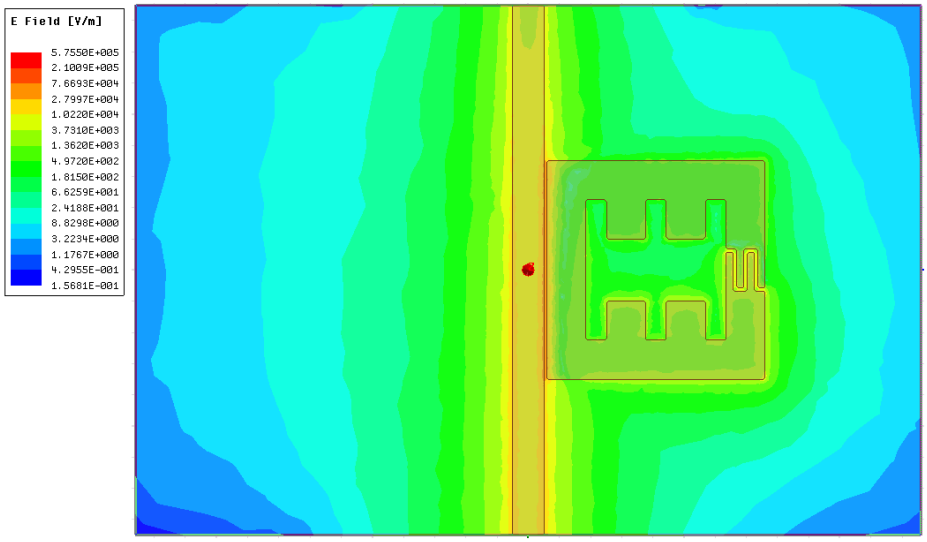

Figure 32: Electric field of the one-sided interdigital centered-gap split-ring resonator in V/m at non-resonance (f=1GHz).

By placing a droplet of the buffer solution in this area, capacitance is influenced strongly which results in a change in resonant frequency. If one microliter of the D3TRIS10-Buffer is placed in the middle of the black rectangle, like it is depicted in Figure 33, the signal is lost due to the formation of a short circuit.

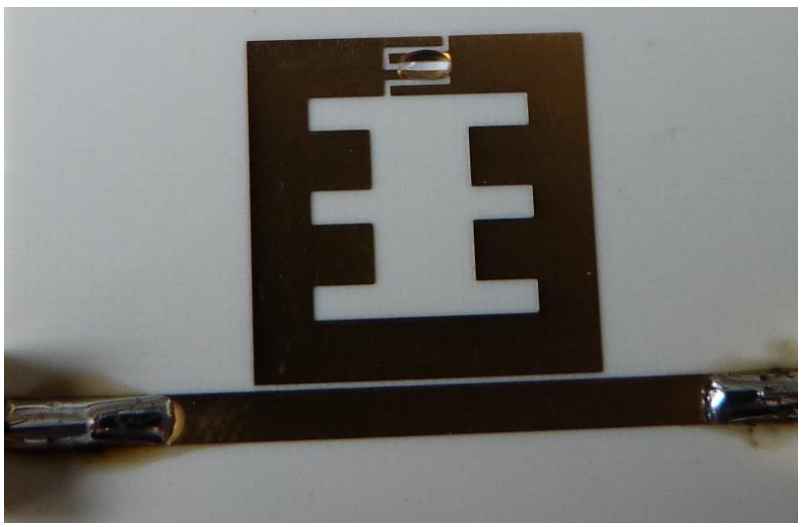

Figure 33: 1µl of buffer D3TRIS10 placed on the sensitive area of the one-sided interdigital centered-gap split-ring resonator.

To avoid the formation of a short circuit, different positions of the buffer droplet are tested experimentally:

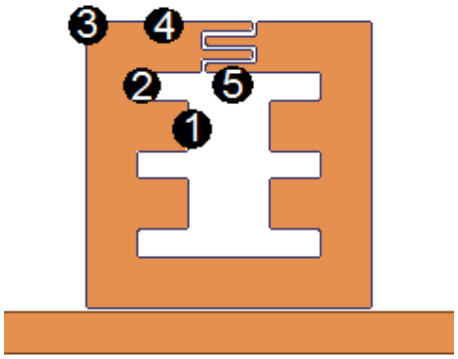

Figure 34: Experimentally tested positions of 1µl D3TRIS10-Buffer on the one-sided interdigital centered-gap split-ring resonator.

The S-parameter S_{21} [dB] are measured with droplets on positions 1 to 5. The results are used to determine the resonant frequency of the loaded structure. Following table shows the resonant frequency f_0 of the unloaded (position 0) and the loaded (positions 1-5) resonator and the resulting frequency shift:

Table 7: Experimentally evaluated frequency shift at different buffer positions.

Position	**0**	**1**	**2**	**3**	**4**	**5**
f_0 [GHz]	1.77946	1.7627	1.771	1.7596	1.7647	1.7321
Δf [MHz]	-	16.76	8.46	19.86	14.76	47.36

The highest frequency shift is achieved at position 5, when the droplet covers the middle of the lower element of the interdigital structure. It accounts for 47.36MHz.

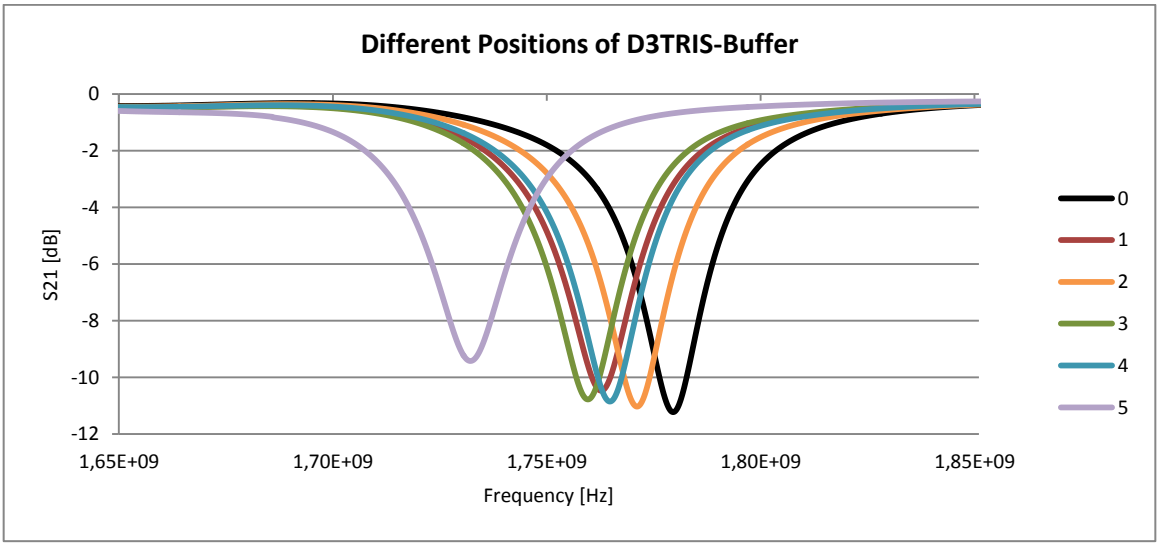

Figure 35: One-sided interdigital centered-gap split-ring resonator without (black) and with 1ul of buffer droplets on different positions (1-5) as depicted in Figure 34

Since all positions of the buffer droplet lead to a measurable frequency shift without generation of a short circuit, compare Figure 35, the position that results in the highest frequency shift, namely position 5, is used for further studies.

5.3. SIMULATION IN HFSS

To further increase the frequency shift, different positions near position 5 (shown in Figure 34), are tested. Since it is difficult to do this experimentally with high accuracy, further simulations in HFSS are performed. The loss tangent of the substrate is assumed to be 0.0055 compare section 4.4. Different parts of the interdigital structure are covered with 1µl of the buffer droplet. The droplet is assumed to be cylindrical with a radius of 1.2mm and a volume of 1µl. The radius was determined using Matlab and a photograph of position 5.

To get significant simulation results, a tab separated data file containing the frequency dependent electromagnetic properties of the D3TRIS10 buffer, which are calculated in section 5.1.2, is built and imported into HFSS. This import file is used to define the material of the droplet. The positions of the basis center of the cylindrical droplets of the buffer are marked by red dots, shown in Figure 36. Position 11 corresponds to position 5 shown in Figure 34. The distance between two centers accounts for 1.3mm.

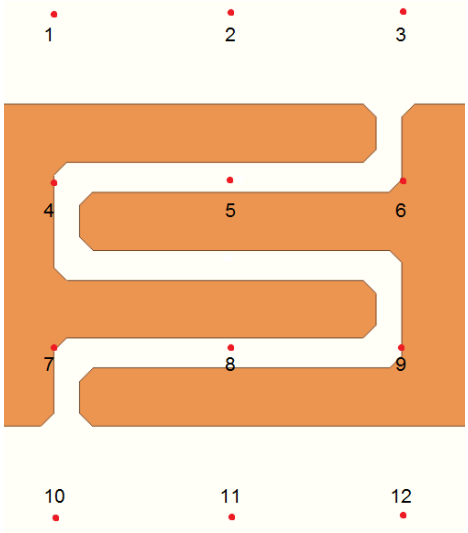

Figure 36: Different positions of the basis center of the buffer droplet marked by red dots.

In total, only four positions provide a measurable frequency shift. The other seven structures lead to a collapse of the signal due to formation of a short circuit. The positions, at which the signal can be measured, are positions 2, 3, 10 and 11.

Following graph shows the S-parameter S_{21} [dB] of the one-sided centered-gap split-ring resonator with 1µl of D3TRIS10 buffer on position 2, 3, 10 and 11 in comparison to the unloaded structure:

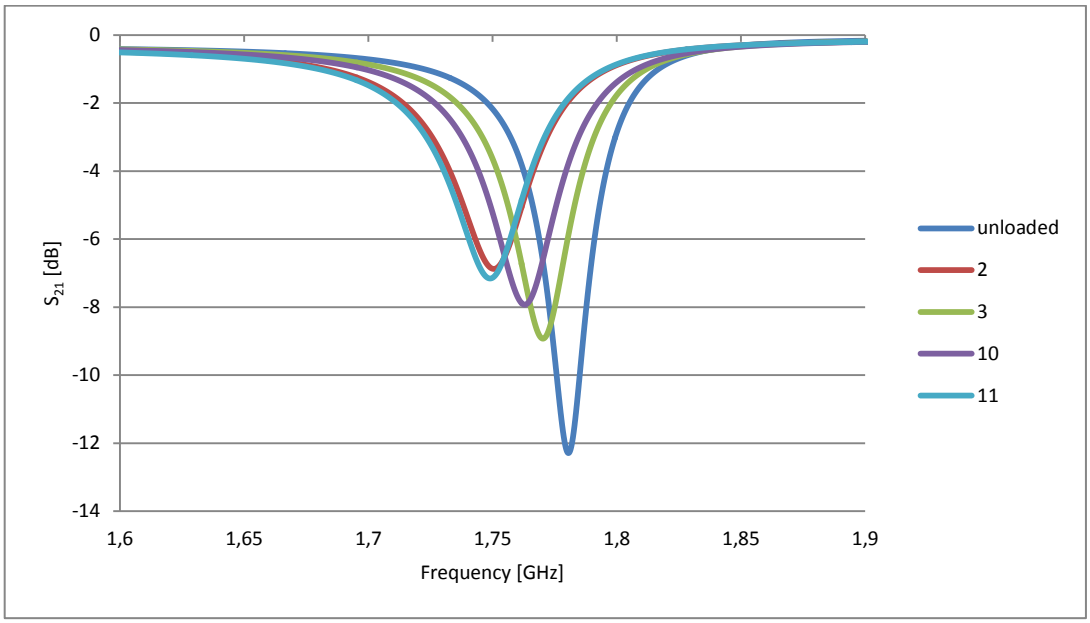

Figure 37: One-sided centered-gap split-ring resonator with 1µl of D3TRIS10 on different positions in comparison to the unloaded structure (blue).

The results of positions 2 and 11 nearly overlap. The reason for this is probably that in both cases the same area is covered, at position 2 at the upper interdigital element and at position 11 at the lower interdigital element. Following table shows the simulated resonant frequency f_0 and the results of the frequency shift Δf in MHz and the percentage frequency shift of the different positions:

Table 8: Frequency shift of different positions of D3TRIS10 evaluated via HFSS.

Position	**unloaded**	**2**	**3**	**10**	**11**
f_0 [GHz]	1.7805	1.7505	1.7702	1.7629	1.749
Δf [MHz]	-	30	10.3	17.6	31.5
Δf [%]	-	1.68	0.58	0.99	1.77

Position 11 provides the highest frequency shift. It accounts for 31.5MHz which corresponds to 1.77%. The frequency shift with position 2 is slightly less and accounts for 30MHz which corresponds to 1.68%.

The same simulations were performed with the carbonate buffer, too. With this buffer, the same four positions lead to measurable results. They are depicted in Figure 38:

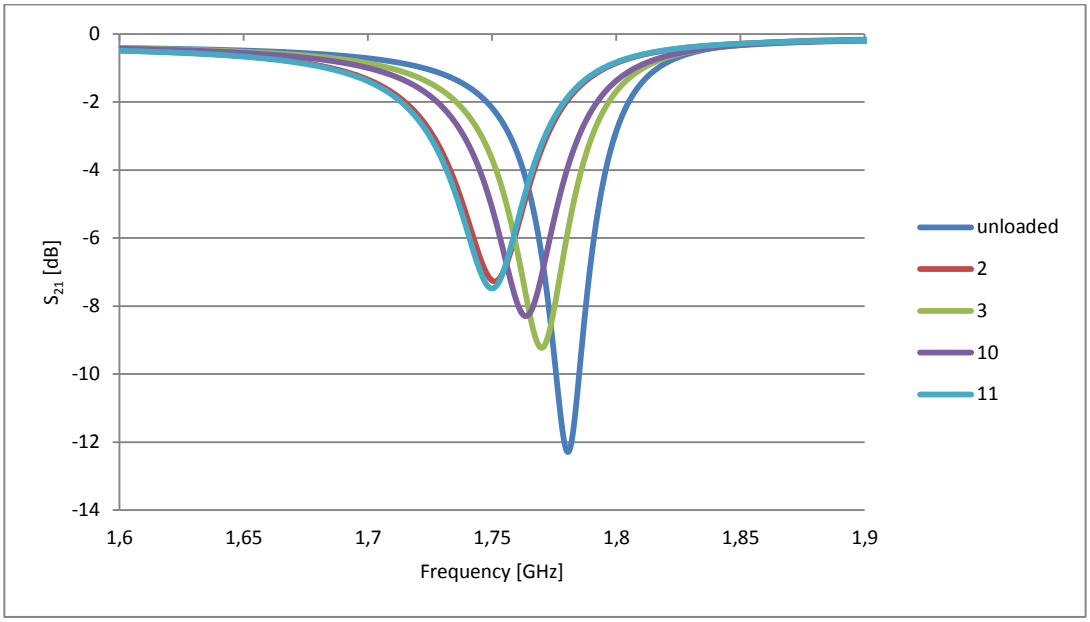

Figure 38: One-sided centered-gap split-ring resonator with 1µl of carbonate buffer on different positions in comparison to the unloaded structure (blue).

Of course, the S-parameters of positions 2 and 11 are almost the same with the carbonate buffer, too. Again, following table shows the simulated resonant frequency f_0 and the results of the frequency shift Δf in MHz and the percentage frequency shift of the different positions:

Table 9: Frequency shift of different positions of carbonate buffer evaluated via HFSS.

Position	**unloaded**	**2**	**3**	**10**	**11**
f_0 [GHz]	1.7805	1.751	1.7699	1.7636	1.7499
Δf [MHz]	-	29.5	10.6	16.9	30.6
Δf [%]	-	1.66	0.6	0.95	1.72

The results differ only slightly from the results of the D3TRIS10 buffer. The reason behind this is that the electromagnetic properties of both buffer solutions are very similar, compare Figure 29.

5.4. FINAL SETUP

After having found a good position for the droplet, Teflon with a dielectric constant of 2.1 is used to construct a housing for the sensor. The upper part of the housing contains a cylindrical recess with a radius of 4.5mm and a height of 0.8mm for a silicone ring. The center of the recess is located at the point where the center of the droplet will be. The silicone ring has a height of 0.8mm. Due to compression of the ring by the housing, the silicone ring functions as seal. Two microfluidic tubes lead to the recess from the outside for supply and removal of the droplet. The upper part of the housing is shown in Figure 39b).

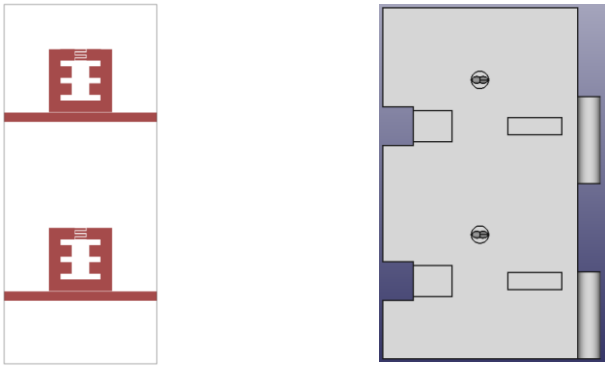

a) **b)**

Figure 39: a) Sensor structure with two sensors, one serving as reference. b) upper part of the housing (view from below).

In the final setup, two resonators will be used, where one serves as reference and the other one will be used for biomolecule binding to determine resonant frequency, compare Figure 39a.

6. RESULTS

A microwave biosensor for measurement of the change of resonant frequency has been developed. A future application can be the detection of biomolecules in human plasma. A model in the high-frequency simulation software HFSS has been set up and validated.

First, a simple split-ring resonator (Figure 1) has been under investigation. It offers a resonant frequency of 2.03GHz. A simulation model has been developed and several simulations have been performed. The simulated resonant frequency accounts for 2.06GHz, which yields a difference to the calculated resonant frequency of 1.5%. The mean error between simulated and measured data is 0.1 and the correlation coefficient accounts for 0.826 with a P-value much less than 0.01 which validates the simulation model, compare Figure 12.

To improve the geometry in terms of a higher quality factor, the resonator width and gap have been varied. The Q-factor increases with decreasing gap size and decreasing resonator width, as it is shown in Figure 40.

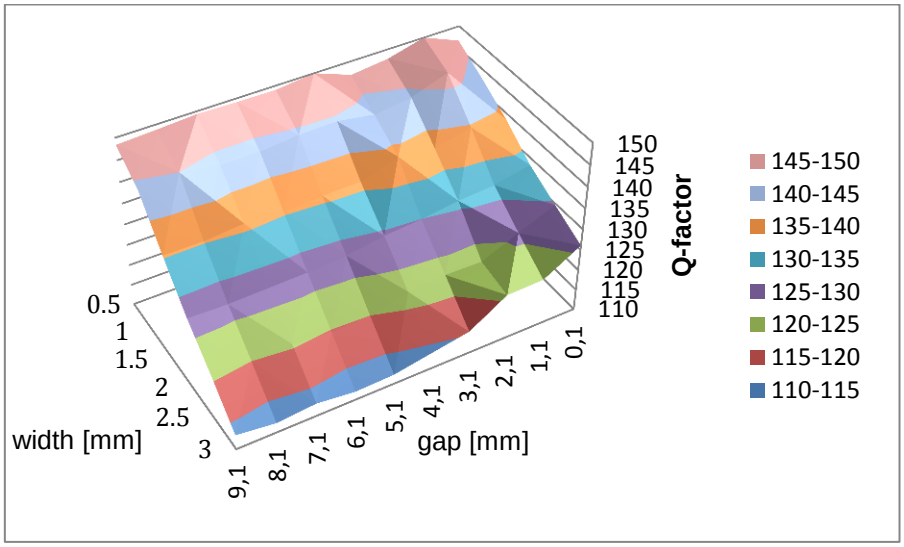

Figure 40: Result of the gap-width variation of the simple SRR.

The highest Q-factor is reached at a gap of 1.1mm and a resonator width of 0.5mm as it is shown in Figure 13. It accounts for 152.7. An even higher Q-factor could be achieved by modifying the geometry. Therefore the centered-gap split-ring resonator (Figure 17A) has been introduced. The highest Q-factor offered by this structure accounts for 254.1 with a gap size of 5mm and a resonator width of 2mm, which is depicted in Figure 18. The capacitance can be further increased by adding an interdigital element to the resonator

which leads to the development of the interdigital centered-gap split-ring resonator (Figure 17B). This structure offers an even higher Q-factor of 257.1226 with a gap of 4mm and a resonator width of 2.5mm, compare Figure 19. The interdigital gap accounts for 0.2mm and the interdigital width is 0.45mm. To save material and cost, the one-sided interdigital centered-gap split-ring resonator is developed. Its Q-factor is slightly lower compared to the two-sided structures. It accounts for 244.564.

Both the one-sided and the two-sided structures where manufactured. After measuring the scattering parameters with a network analyzer, the results where compared to the simulations, Figure 20 and Figure 21. For the two-sided interdigital centered-gap split-ring resonator, a correlation coefficient of 0.816 and a P-value of 0 have been calculated. The simulated resonant frequency differs from the measured resonant frequency by only 0.7%. The mean error between measurement and calculation accounts for 0.02. For the one-sided structure, the correlation coefficient accounts for 0.461 with a P-value of 0. The resonant frequency of the simulation differs from the measurement by only 0.1% and the mean error accounts for 0.1. To get a better match between the manufactured structure and the simulation model, the loss tangent is varied in the simulations. An increased loss tangent of 0.0055 is found to provide the best match between simulation and measurement. Using this loss tangent in the simulations, the resulting resonant frequency accounts for 1.7805GHz which yields a percentage error of 0.584% and the Q-factor accounts for 158.4855 which corresponds to a percentage error of 2.0494%. The correlation coefficient accounts for 0.996 with a P-value of 0. The forward transmission coefficients of the measured and simulated structure are illustrated in Figure 41.

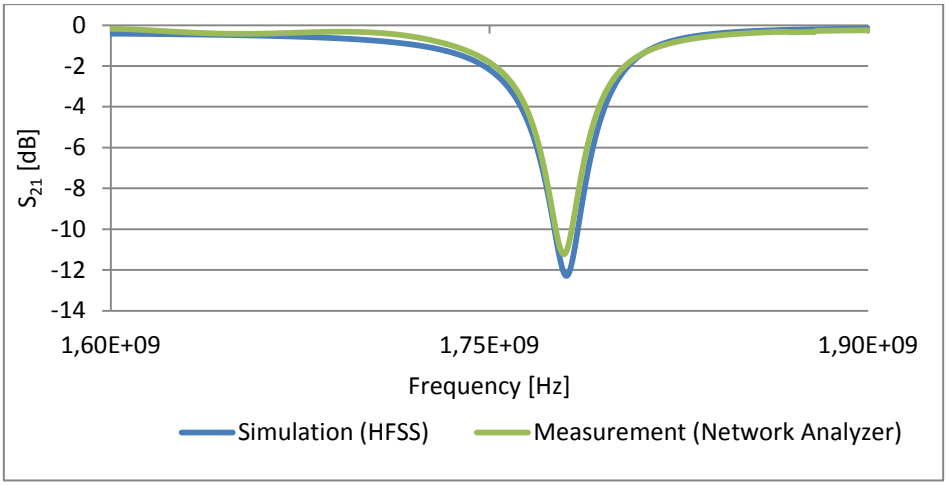

Figure 41: Comparison of the measured (green) and simulated (blue) S-parameter S_{21} of the interdigital centered-gap split-ring resonator placed only on one side of the microstrip line with a loss tangent of 0.0055.

An equivalent circuit containing resistive, capacitive and inductive elements for the one-sided interdigital centered-gap split-ring resonator has been developed and adjusted to the structure (Figure 26). The total mean error between the equivalent circuit and the manufactured resonator accounts for 0.03.

After having found a structure that offers a very high quality, the one-sided interdigital centered-gap split-ring resonator has been chosen to be under further investigation. A position for the fluid under test has to be found that yields a measureable shift of resonant frequency without collapse of the signal. In order to do this, different buffer solutions have been characterized in terms of their permittivity, conductivity and loss tangent (Figure 29). The 'Principle of Reflection Method' has been used to measure complex permittivity. The method has been validated by comparing the measured complex permittivity of 98% Ethanol to values found in literature. A t-test has been performed with the result that there is no significant difference between the measured values and the values found in literature with a level of significance of 0.05.

Experimentally, different positions of the buffer droplet on the split-ring resonator have been tested (Figure 34). As expected, the position that offers the highest frequency shift covers a part of the interdigital structure. In HFSS, simulations were performed to further vary the position of the buffer droplet to improve the signal as shown in Figure 36. The position which shows the highest shift in resonant frequency without formation of a short circuit is shown in Figure 42.

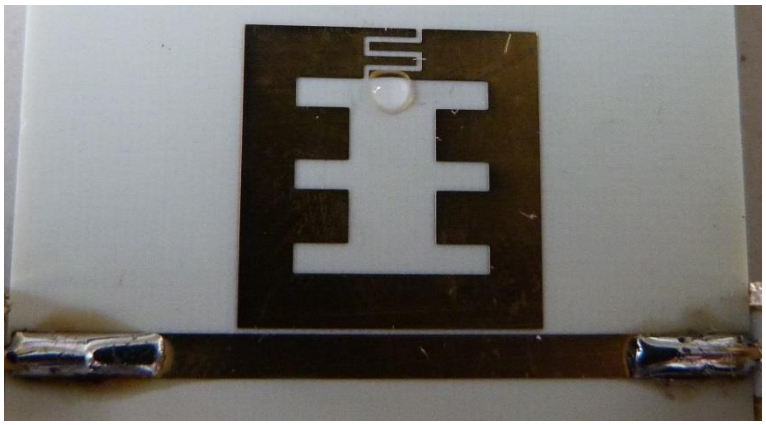

Figure 42: 1µl of buffer placed on the position which provides the highest frequency shift without formation of a short circuit.

The found position shown in the figure above offers a frequency shift of 31.5MHz which accounts for 1.77% for the D3TRIS10 buffer and a frequency shift of 30.6MHz which accounts for 1.72% for the carbonate buffer, compare Figure 37 and Table 8 for the TRIS buffer and Figure 38 and Table 9 for the carbonate buffer. The shift of resonant frequency is depicted in Figure 43 which shows the forward transmission factor of the unloaded sensor and the sensor loaded with 1µl of the D3TRIS10 and 1µl of the carbonate buffer, respectively.

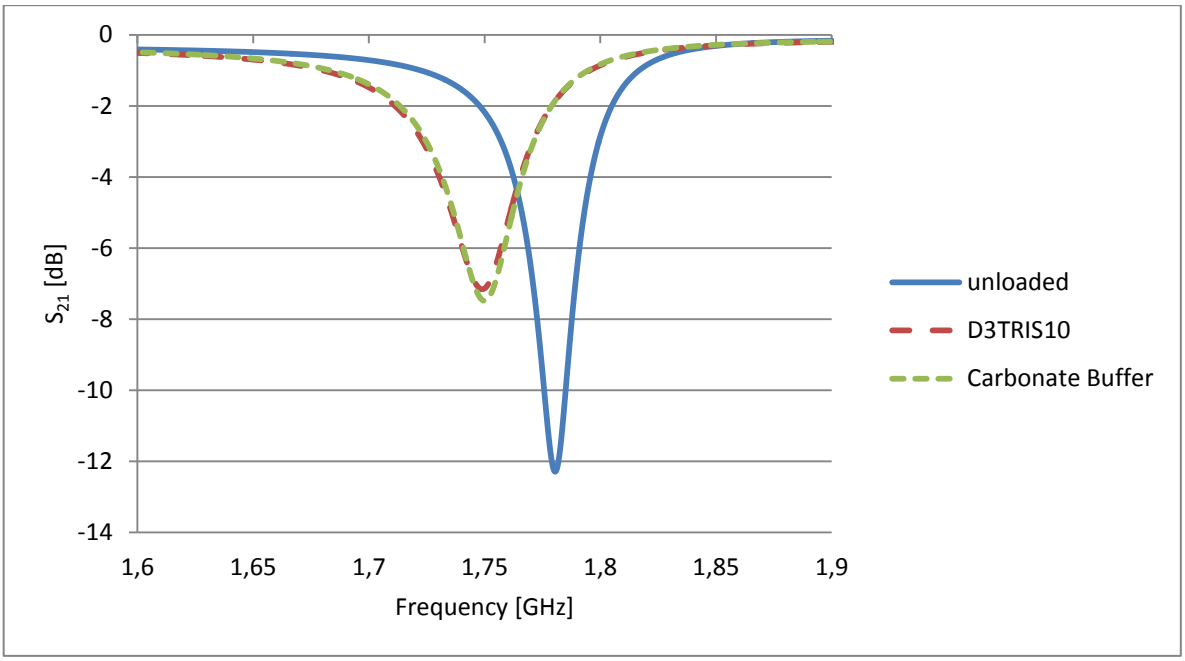

Figure 43: Forward transmission factor of the unloaded interdigital centered-gap SRR (blue), loaded with 1µl of D3TRIS10 (red) and 1µl of carbonate buffer (green) simulated in HFSS.

As described in section 5.4, two resonators will be used in the final setup which is not developed yet. One will serve as reference and the other one will be used for biomolecule binding to determine the shift in resonant frequency, compare Figure 44.

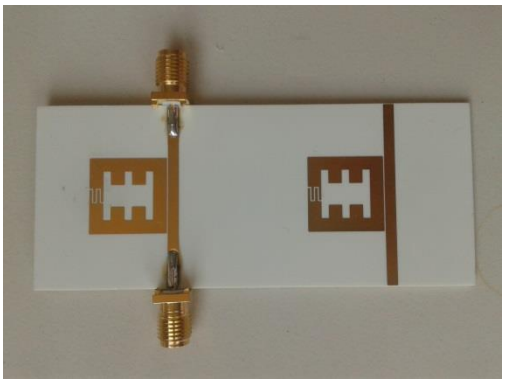

Figure 44: Manufactured structure for final setup.

7. DISCUSSION

There is a wide range of applications using split-ring resonators as sensors. They have already been used as strain sensors by measuring the frequency shift which is correlated with the surface strain of the test material [37], as pressure sensors [38] and as displacement sensors [39]. Additionally, applications as moisture sensors have been reported [40].

The application of split-ring resonators with different geometries as biosensors has been under investigation in former works, too. They were used to detect e.g. prostate specific antigen or cortisol stress hormone [6]. Additionally, ethanol-water and methanol-water mixtures with different concentrations have been used to validate the sensor principle [20].

The geometry used in [20] is a simple SRR as shown in Figure 1 providing a quality factor of 130. In [6], the structure of the sensor of the simple split-ring resonator is modified: a second SRR is placed in the middle of the simple SRR. This geometry provides a quality factor of 50.

In this work, a high sensitive split-ring resonator providing a measurable resonant frequency shift of 30MHz due to addition of two different buffer solutions has been developed. The quality factor of the unloaded split-ring resonator accounts for about 155 which is higher than the quality factor in the publications mentioned above. The frequency shift in [6] accounts up to an average of 30MHz which equals the shift in this work.

The next step regarding the development of a biosensor should be the build-up of a microfluidic system for the supply and removal of the fluid under test. An oscillator should be designed to get the difference frequency between the reference and the sensing resonator.

8. PUBLICATIONS

[I] T. Voglhuber-Brunnmaier., L.-M. Wagner, C. G. Diskus, B. Jakoby, M. Brandl, "Sensitivity Optimization of Microwave Biosensors." Procedia Engineering 168 (2016): 634-637.

[II] M. Brandl, L.-M. Wagner, J. Agbodjan Prince, M. Wellenzohn, "A microwave split ring resonator (SRR) with hydrogel based biofunctionalziation for sensor applications.", Poster Presentation at BIOSENSORS 2016, Gothenburg.

[III] L.-M. Wagner, T. Voglhuber-Brunnmaier, M. Brandl, "Optimization of a Biosensor Device based on a microwave Split-Ring Resonator.", Poster Presentation at MNE 2016, Vienna.

[IV] L.-M. Wagner, F. Strasser, E. Melnik, M. Brandl, "Electromagnetic Characterization and Simulation of Carbonate Buffer System on a Microwave Biosensor.", Poster Presentation at Eurosensors2017, Paris.

[V] L.-M. Wagner, F. Strasser, E. Melnik, M. Brandl, "Electromagnetic Characterization and Simulation of Carbonate Buffer System on a Microwave Biosensor.", Proceedings of the Eurosensors2017, submitted.

REFERENCES

[1] T. Chen, S. Li and H. Sun, "Metamaterials Application in Sensing," *Sensors,* vol. 12, no. 3, pp. 2742-2765, 2012.

[2] J. H. Lee, K. S. Hwang, J. Park, K. H. Yoon, D. S. Yoon and T. S. Kim, " Immunoassay of prostate-specific antigen (PSA) using resonant frequency shift of piezoelectric nanomechanical microcantilever," *Biosensors and Bioelectronics*, vol. 20, no. 10, pp. 2157-2162, 2005.

[3] J. Homola, S. S. Yee and G. Gauglitz, "Surface plasmon resonance sensors," *Sensors and Actuators B: Chemical,* vol. 54, no. 1, pp. 3-15, 1999.

[4] C. Zhang, R. Wang, C. Min, S. Zhu and X. C. Yuan, " Experimental approach to the microscopic phase-sensitive surface plasmon resonance biosensor," *Applied Physics Letters,* vol. 102, no. 1, p. 011114, 2013.

[5] G. Zheng, F. Patolsky, Y. Cui, W. U. Wang and C. M. Lieber, "Multiplexed electrical detection of cancer markers with nanowire sensor arrays," *Nature biotechnology*, vol. 23, no. 10, p. 1294, 2005.

[6] H. J. Lee, J. H. Lee, H. S. Moon, I. S. Jang, J. S. Choi, J. G. Yook and H. I. Jung, "A planar split-ring resonator-based microwave biosensor for label-free detection of biomolecules," *Sensors and Actuators B: Chemical,* vol. 169, pp. 26-31, 2012.

[7] T. Reinecke, J.-G. Walter, T. Kobelt, A. Ahrens, T. Scheper and S. Zimmermann, "Biosensor based on a split-ring resonator," *Proceedings of the Sensors 2017,* pp. 78-83, 2017.

[8] M. Wellenzohn and M. Brandl, "A theoretical design of a biosensor device based on split ring resonators for operation in the microwave regime," *Procedia Engineering*, vol. 120, pp. 865-869, 2015.

[9] C. Y. Chao and L. J. Guo, "Biochemical sensors based on polymer microrings with sharp asymmetrical resonance," *Applied Physics Letters,* vol. 83, no. 8, pp.

1527-1529, 2003.

[10] R. Zajicek, L. Oppl and J. Vrba, "Broadband measurement of complex permittivity using reflection method an coaxial probes," *Radioengineering*, pp. 14-19, April 2008.

[11] G. Lehner, Elektromagnetische Feldtheorie, Springer-Verlag Berlin Heidelberg, 2009.

[12] J. D. Jackson, K. Müller, C. Witte and M. Diestelhorst, Klassische Elektrodynamik, Berlin; Boston: Walter de Gruyter, 2014.

[13] W. Cai and V. Shalaev, Optical Metamaterials, New York: Springer-Verlag New York, 2010.

[14] J. Krupka, J. Breeze, A. Centeno, N. Alford, T. Claussen and L. Jensen, "Measurements of Permittivity, Dielectric Loss Tangent and Resisitivity of Float-Zone Silicon at Microwave Frequencies," *IEEE Transactions on microwave theory and techniques* , pp. 3995-4001, December 2006.

[15] E. Böhmer, Elemente der Angewandten Elektronik, Braunschweig: Friedr. Vieweg & Sohn Verlagsgesellschaft mbH, 1986.

[16] S. Paul and R. Paul, Grundlagen der Elektrotechnik und Elektronik 2 : Elektromagnetische Felder und ihre Anwendungen, Berlin, Heidelberg: Springer Berlin Heidelberg, 2012.

[17] A. J. Schwab, Begriffswelt der Feldtheorie : Elektromagnetische Felder, Maxwell-Gleichungen, Gradient, Rotation, Divergenz, Berlin, Heidelberg: Springer Berlin Heidelberg, 2013.

[18] H. Heuermann, Hochfrequenztechnik : Lineare Komponenten hochintegrierter Hochfrequenzschaltungen, Wiesbaden: Vieweg, 2005.

[19] G. Gonzalez, Microwave transistor amplifiers: analysis and design, Prentice-Hall, Inc., 1996.

[20] W. Withayachumnankul, K. Jaruwongrungsee, A. Tuantranont, C. Fumeaux and D. Abbott, "Metamaterial-based microfluidic sensor for dielectric characterization," *Sensors and Actuators A: Physical,* vol. 189, pp. 233-237, 2013.

[21] R. A. Shelby, D. R. Smith and S. Schultz, "Experimental verification of a negative index of refraction," *Science,* vol. 292, no. 5514, pp. 77-79, 2001.

[22] M. J. Lockyear, A. P. Hibbins and J. R. Sambles, "Microwave surface-plasmon-like modes on thin metamaterials," *Physical Review Letters,* vol. 102, no. 7, pp. 073901-1-073901-4, 2009.

[23] J. Pendry, L. Martin-Moreno and F. Garcia-Vidal, "Mimicking surface plasmons with structured surfaces," *Science (New York, N.Y.),* vol. 305, no. 5685, pp. 847-848, 2004.

[24] E. Melnik, F. Strasser, P. Müllner, R. Heer, G. C. Mutinati, G. Koppitsch, P. Lieberzeit, M. Lämmerhofer and R. Hainberger, "Surface Modification of Integrated Optical MZI Sensor Arrays Using Inkjet Printing Technology," *Procedia Engineering,* vol. 168, pp. 337-340, 2016.

[25] F. Strasser, E. Melnik, P. Muellner, P. Jiménez-Meneses, M. Nechvile, G. Koppitsch, P. Lieberzeit, M. Laemmerhofer, R. Heer and R. Hainberger, "Preparation of Mach-Zehnder interferometric photonic biosensors by inkjet printing technology," *SPIE Optics+ Optoelectronics,* pp. 102312H-102312H-7, 2017.

[26] E. Melnik, P. Muellner, O. Bethge, E. Bertagnolli, R. Hainberger and M. Laemmerhofer, "Streptavidin binding as a model to characterize thiol–ene chemistry-based polyamine surfaces for reversible photonic protein biosensing," *Chemical Communications,* vol. 50, no. 19, pp. 2424-2427, 2014.

[27] E. Melnik, P. Muellner, G. C. Mutinati, G. Koppitsch, F. Schrank, R. Hainberger and M. Laemmerhofer, "Local functionalization of CMOS-compatible Si 3 N 4 Mach-Zehnder interferometers with printable functional polymers," *Sensors and Actuators B: Chemical,* vol. 236, pp. 1061-1068, 2016.

[28] S. Sam, L. Touahir, J. Salvador Andresa, P. Allongue, J.-N. Chazalviel, A. C. Gouget-Laemmel, C. Henry De Villeneuve, A. Moraillon, F. Ozanam, N. Gabouze and S. Djebbar, "Semiquantitative study of the EDC/NHS activation of acid terminal groups at modified porous silicon surfaces," *Langmuir*, vol. 26 , no. 2, pp. 809-814, 2010 .

[29] M. Brandl, L.-M. Wagner, J. Agbodjan Prince, E. Melnik and M. Wellenzohn, "A microwave split ring resonator (SRR) with hydrogel based biofunctionalization for sensor applications," in *Poster Presentation at MNE*, Gothenburg, 2016.

[30] I. M. Rusni, A. Ismail, A. R. H. Alhawari, M. N. Hamidon and N. A. Yusof, "An aligned-gap and centered-gap rectangular multiple split ring resonator for dielectric sensing applications.," *Sensors*, vol. 14, no. 7, pp. 13134-13148, 2014.

[31] L.-M. Wagner, T. Voglhuber-Brunnmaier and M. Brandl, "Optimization of a Biosensor Device based on a Microwave Split-Ring Resonator," in *Poster Presentation at MNE*, Vienna, 2016.

[32] L.-M. Wagner, F. Strasser, E. Melnik and M. Brandl, "Electromagnetic Characterization and Simulation of Carbonate Buffer System on a Microwave Biosensor," in *Poster Presentation at Eurosensors*, Paris, 2017.

[33] A. Gregory and R. N. Clarke, Tables of the complex permittivity of dielectric reference liquids at frequencies up to 5GHz, Teddington, UK: National Physical Laboratory, 2001.

[34] J. K. M. Aps and L. C. Martens, "Review: The physiology of saliva and transfer of drugs into saliva," *Forensic Science International*, vol. 150, no. 2, pp. 119-131, 2005.

[35] K. M. Hold, D. d. Boer, J. Zuidema and R. A. Maes, "Saliva as an analytical tool in toxicology," *Int J Drug Test*, vol. 1, no. 1, pp. 1-36, 1996.

[36] S. Chiappin, G. Antonelli, R. Gatti and E. F. D. Palo, "Saliva Specimen: A New Laboratory Tool for Diagnostic and Basic Investigation," *Clinica Chimica*, vol. 383, no. 1, pp. 30-40, 2007.

[37] R. Melik, E. Unal, N. K. Perkgoz, C. Puttlitz and H. V. Demir, "Metamaterial-based wireless strain sensors," *Applied Physics Letters*, vol. 95, no. 1, p. 011106, 2009.

[38] P. K. Pattnaik, B. Vijayaaditya, T. Srinivas and A. Selvarajan, "Optical MEMS pressure sensor using ring resonator on a circular diaphragm," *International Conference on MEMS, NANO and Smart Systems Proceedings,* pp. 277-280, 2005.

[39] X. Liu, C. Xue, S. Yan, J. Xiong and W. Zhang, "Integrated high sensitivity displacement sensor based on micro ring resonator," *4th IEEE International Conference on Nano/Micro Engineered and Molecular Systems,* pp. 1000-1003, 2009.

[40] R. A. Yogi, R. S. Parolia, R. N. Karekar and R. C. Aiyer, "Microwave Microstrip ring resonator as a paper moisture sensor: Study with different grammage," *Measurement Science and Technology,* vol. 13, no. 10, pp. 1558-1562, 2002.